EYE-CLIMA
Verifying emissions of climate forcers

Fluxes of CO_2 and CH_4 for Russia

DELIVERABLE 3.5

Author(s):	Rona Thompson (NILU), Rebecca Ward (FMI)
Date of submission:	02-03-2026
Version:	1.0
Responsible partner:	FMI
Deliverable due date:	31-12-2025
Dissemination level:	Public

Call:	HORIZON-CL5-2022-D1-02
Topic:	Climate Sciences and Responses
Project Type:	Research and Innovation Action
Lead Beneficiary:	NILU - Norsk Institutt for Luftforskning

This project has received funding from the European Union's Horizon Europe research and innovation programme under grant agreement No 101081395

Document History

Version	Date	Comment	Modifications made by
0.1	25-02-2026	First draft	Rona Thompson (NILU), Rebecca Ward (FMI)
0.2	26-02-2026	Internal review	Gregoire Broquet (CNRS)
0.3	28-02-2026	Final draft	Rona Thompson (NILU), Rebecca Ward (FMI)
1.0	02-03-2026	Submitted to Commission	Rona Thompson (NILU)

This project has received funding from the European Union's Horizon Europe research and innovation programme under grant agreement No 101081395

Summary

The aim of this deliverable is to demonstrate the transferability of the atmospheric inversion methods developed in EYE-CLIMA to a region outside of EU Europe. The region chosen for this case study is Russia. Russia is an interesting region to study in terms of its methane (CH_4) emissions and its land-biosphere fluxes of carbon dioxide (CO_2). Russia has the world's largest natural gas reserves as well as abundant oil and coal reserves and is one of the world's leading producers of gas and crude oil. It also has large expanses of high latitude peatlands. In addition, Russia has the largest expanse of Boreal forest covering about one quarter of its territory, which is thought to be an important sink of CO_2.

In this study, two atmospheric inversion frameworks are used to estimate the fluxes of CH_4 and CO_2 over Russia for the period 2015 to 2021. For CO_2, the inversions were run with the inversion framework, FLEXINVERT, and for CH_4, they were run using CTE-CH_4.

The inversions for CO_2 only optimized the land biosphere fluxes, specifically, the net ecosystem exchange and land-use change fluxes, NEE + F_{LUC}. The inversion indicated a decrease in the carbon sink with respect to the prior estimates with an annual mean sink for 2015 to 2021 of -0.75 ± 0.13 $PgCO_2$/y (-0.20 ± 0.04 PgC/y). Sensitivity tests conducted for the year 2015, examined the impact of changing prior NEE, fossil emissions and harvest fluxes. The range of these tests was -0.81 – -0.64 $PgCO_2$/y. Moreover, when the NEE + F_{LUC} is adjusted to account for the harvest fluxes, the sink is reduced further, and depending on the harvest fluxes used, could be a sink of around -0.21 $PgCO_2$/y or nearly carbon neutral.

For CH_4, the inversion indicates a modest increase in the total source for Russia 2015 to 2021 (2.8%) with respect to the prior estimates. However, this masks larger sectoral differences: agriculture plus waste and combustion emissions increase more substantially (by 9.0% and 7.8%, respectively), while increases in wetland and freshwater and fugitive fossil fuel emissions are smaller. Monthly emissions show a pronounced seasonal cycle dominated by wetland fluxes, with an annual peak in July. Smaller but important contributions are shown from the biomass burning sector and winter peaks in the anthropogenic sectors. Spatially, wetland emissions remain the principal source in northern Russia, while anthropogenic sources dominate in the south.

This project has received funding from the European Union's Horizon Europe research and innovation programme under grant agreement No 101081395

TABLE OF CONTENTS

This project has received funding from the European Union's Horizon Europe research and innovation programme under grant agreement No 101081395

1. Introduction

Russia is the world's largest country by area and extends from Eastern Europe to the Pacific Ocean. It covers numerous climate zones from sub-tropical along the coast of the Black Sea to Arctic tundra in the north. Russia has the world's largest natural gas reserves as well as abundant oil and coal reserves and is one of the world's leading producers of gas and crude oil[1]. Russia also has the largest expanse of Boreal forest covering about one quarter of its territory, which is an important sink of carbon dioxide (CO_2) sequestering an estimated 1.97 ± 0.81 $PgCO_2$/yr (equivalent to 0.54 ± 0.22 PgC/yr) (Shvidenko et al., 2025) . It's large fossil energy production and important Boreal ecosystem make Russia a very important country in determining the global budgets of methane (CH_4) and CO_2 (Friedlingstein et al., 2025; Saunois et al., 2025) . Despite this, Russia's CH_4 and CO_2 budgets remain very uncertain.

Since the collapse of the USSR, Russia has reported almost no change in forested area and forest biomass to the UNFCCC whereas satellite remote sensing indicates increased tree cover and biome productivity (Schepaschenko et al., 2021; Yang et al., 2023) . This apparent greening trend is reported to be due to warming, lengthening of the growing season, increasing atmospheric CO_2 (Piao et al., 2007) , and also due to reforestation of abandoned arable land. A recent study involving several atmospheric inversions also found an increase in the carbon sink in Russia from 2000-2019 (Shvidenko et al., 2025).

Russia is one of the countries with the largest CH_4 emissions with around 21 to 23 $TgCH_4$/yr (range of top-down and bottom-up estimates) from direct anthropogenic sources, especially in the energy sector (Saunois et al. 2025). In addition, Russia has a large natural CH_4 source estimated to be between 14 and 25 $TgCH_4$/y, with a large contribution from peatlands (Saunois et al. 2025).

To support emission mitigation efforts, such the Global Methane Pledge, it is important to better quantify the actual anthropogenic emissions of CH_4 and their trends. Additionally, it is important to have improved estimates of CH_4 emissions from natural sources, as these are susceptible to climate change. In particular, northern peatland emissions of CH_4 may be increasing with warmer temperatures and more precipitation. The Arctic has warmed by approximately 0.75°C per decade since 1980 and precipitation has increased by 4.5% per °C (Bintanja et al., 2020; Rantanen et al., 2022) . Warmer temperatures are also leading to peatland permafrost thaw, which could release further CH_4 into the atmosphere.

Atmospheric inversion is a method to improve estimates of surface-atmosphere fluxes using observations of atmospheric mixing ratios, in this case of CO_2 and CH_4. It involves using a model of atmospheric transport to relate surface fluxes to atmospheric mixing ratios, and statistical optimization methods, to use the model-observation discrepancy to correct a prior (or first guess) estimate of the fluxes.

This deliverable describes the methodology used to estimate fluxes of CO_2 from the land-biosphere, i.e., net biome production (NBP), and fluxes of CH_4 for Russia, and presents the results for the period from 2015 to 2021. Unfortunately, more recent estimates could not be obtained owing to the inaccessibility of ground-based observations in Russia since the invasion of Ukraine in February 2022.

[1] https://www.bp.com/content/dam/bp/business-sites/en/global/corporate/pdfs/energy-economics/statistical-review/bp-stats-review-2020-full-report.pdf

This project has received funding from the European Union's Horizon Europe research and innovation programme under grant agreement No 101081395

2. Methodology

Two different atmospheric inversion tools are used in this deliverable, FLEXPART-FLEXINVERT for CO_2, and CarbonTracker Europe (CTE) for CH_4. Although these are different systems, both are based on Bayesian statistics and find the fluxes that minimise the distance between the modelled and observed mixing ratios and the distance from a prior estimate of the fluxes. This is described by the following cost function:

$$J(\mathbf{x}) = \frac{1}{2}(\mathbf{x}-\mathbf{x_b})^T\mathbf{B}^{-1}(\mathbf{x}-\mathbf{x_b}) + \frac{1}{2}\big(\mathbf{y}-H(\mathbf{x})\big)^T\mathbf{R}^{-1}\big(\mathbf{y}-H(\mathbf{x})\big) \quad (1)$$

Where $\mathbf{x_b}$ and $\mathbf{x}$ are the prior and optimized (i.e. posterior) estimate of the fluxes, $\mathbf{y}$ is a vector of observed mole fractions. $\mathbf{B}$ is the prior error covariance matrix and describes, to the best knowledge, the uncertainty of the prior fluxes and its covariance between flux variables. $\mathbf{R}$ is the observation error covariance matrix and describes the uncertainty in the observations, but also in the ability of the atmospheric transport model and model set-up to represent the observations. The function $H(\mathbf{x})$ represents the atmospheric transport and any chemistry and relates the fluxes to mole fractions.

The two atmospheric inversion tools are described below, including the atmospheric transport model, prior fluxes, and other input data.

2.1 CO_2 inversions

The methodology for the CO_2 inversions adheres as closely as possible to that used for the European CO_2 inversions for deliverables 3.2 and 3.4 and is briefly described below.

2.1.1 FLEXPART-FLEXINVERT

FLEXPART-FLEXINVERT is the combination of the Lagrangian Particle Dispersion Model, FLEXPARTv11 (Bakels et al., 2024) and the Bayesian inversion framework, FLEXINVERT (Thompson and Stohl, 2014) .

FLEXPART models atmospheric transport using virtual particles that are subject to dispersion and advection. For inverse modelling, FLEXPART is run in a backwards time mode in which the particles are released from an observation point (receptor) and their trajectories are traced backwards in time for up a number of days (in this study 10 days). The residence times of these particles in grid cells at the surface are used to define a so-called source-receptor-relationship (SRR). The SRR describes the relationship between a change in a flux at the surface and the change in mole fraction at the receptor and this study was computed at 3-hourly intervals and at 0.5° × 0.5° for the inversion domain (180°W to 180°E and 41°N to 82°N) and at 2.0° × 2.0° globally. In addition, FLEXPART calculates a so-called background-receptor-relationship (BRR) which describes the dependence of the mole fraction at the receptor on the mole fraction in any given grid cell in 3D space at the time of the termination of the backwards trajectories and in this study is saved at 2.0° × 2.0° globally and for 12 vertical levels.

FLEXINVERT simulates atmospheric mole fractions using the FLEXPART SRRs at 0.5° × 0.5° and 3-hourly temporal resolution and a given estimate of the fluxes. In addition, FLEXINVERT estimates the background mole fraction, i.e., the contribution from fluxes outside the inversion domain and from the mole fractions where the particle trajectories terminated. This is calculated using the global SRRs and a global flux estimate (minus the inversion domain), and the BRRs and a 3D global CO_2 mixing ratio field.

In this study, the state vector consists of offsets to the Net Ecosystem Exchange (NEE) plus Land-use Change (LUC) fluxes and the ocean fluxes as well as scalars of the initial mixing ratios used in the boundary conditions. Other flux components (fossil fuel and cement emissions, harvest emissions, biomass burning emissions, and inland water fluxes) are not optimized but are accounted for when simulating atmospheric CO_2. The production of CO_2 from atmospheric oxidation of CO is ignored as this was shown to be negligible (EYE-CLIMA Milestone 3) and the sink of CO_2 from rock weathering is very small (~0.35 $PgCO_2$/y globally, (Berner and Caldeira, 1997)) and thus is also ignored.

This project has received funding from the European Union's Horizon Europe research and innovation programme under grant agreement No 101081395

The NEE flux offsets are optimized for 6-hourly intervals that are averaged over 28 days. The 6-hourly intervals are for [0-6), [6-12), [12-18) and [18-24) hours and are defined for the local time of each grid cell. The ocean flux offsets are optimized for 28-day intervals. The state variables corresponding to flux offsets are defined on a variable spatial grid that is based on the SRRs and prior fluxes following the method of Thompson and Stohl (2014) (see Fig. 2.1.1). This grid has finer resolution where the NEE fluxes have a stronger influence on the observed CO_2 mole fractions and vice-versa.

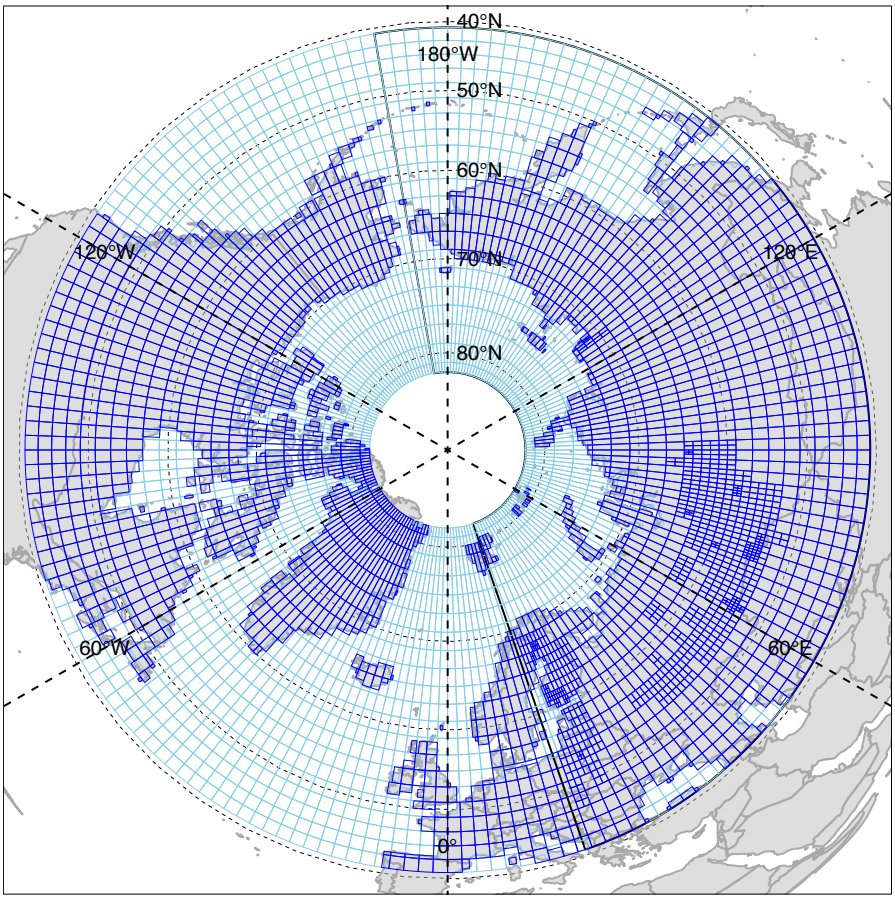

***Figure 2.1.1**. Map showing the inversion domain and the variable spatial grid used for the inversion (dark blue for land and light blue for sea). The region of interest encompassing all of Russia (19°E to 170°W and 41°N to 82°N) is outlined in black.*

2.1.2 Prior fluxes and their uncertainties

In the inversion, only NEE and land use change fluxes (NEE + F_{LUC}), and the ocean fluxes, are optimized. All other CO_2 fluxes are fixed components, that is those due to wildfires, crop and wood source, inland waters, fossil fuel combustion and cement manufacture.

The land C budget can be summarized as follows:

$$NBP = NEE + F_{LUC} + F_{fire} \quad (2)$$

$$\Delta C = NBP + F_{crop} + F_{wood} + F_{river} + F_{lake} \quad (3)$$

Where NEE + F_{LUC} is optimized while F_{crop}, F_{wood}, F_{fire}, F_{river} and F_{lake} (and F_{fossil}) are fixed components.

This project has received funding from the European Union's Horizon Europe research and innovation programme under grant agreement No 101081395

NEE + LUC

For NEE + F_{LUC} the estimates from the ORCHIDEE global land biosphere model are used. These fluxes were prepared in the framework of Work Package 2. ORCHIDEE was forced with meteorological data from the dataset, CRUJRA v2.5, which consists of the JRA-55 (Japanese 55-year Reanalysis) merged with the CRU TS dataset (i.e. temperature, shortwave radiation and precipitation are aligned with CRU). NEE is provided at 3-hourly resolution while LUC is provided at daily resolution and both variables have 0.5° spatial resolution. NEE is the sum of gross primary production, ecosystem autotrophic and heterotrophic respiration fluxes with negative values indicating a sink of CO_2.

Harvest emissions

Harvest emissions, i.e., F_{crop} and F_{wood} are from the ORCHIDEE model with daily temporal and 0.5° spatial resolution. ORCHIDEE attributes these fluxes to the same model grid cell as the carbon was sequestered, specifically it calculates the harvest fluxes as a fraction of NEE in croplands and managed forests, respectively. Therefore, these fluxes components were spatially redistributed using the lateral flux data product (version 6) of (Ciais et al., 2020) but keeping the mass balance of the ORCHIDEE estimates. The lateral flux product has a spatial resolution of 5 minutes (0.083°) and was averaged to 0.5° to match the resolution of ORCHIDEE. Sensitivity tests were also carried out to examine how sensitive the results were to changing the spatial distribution and magnitude of the harvest emissions (see Section 2.1.4).

Fossil fuel and cement emissions

The fossil fuel and cement emissions estimates were from the Emissions Database for Global Atmospheric Research (EDGARv8) as recommended through the evaluation in Work Package 2 (Milestone 2). EDGARv8 provides global emission maps at 0.1° resolution and monthly for 8 sectors: agriculture, energy for buildings, fuel exploitation, industrial combustion, industrial processes (including cement manufacture), power, transport, and waste. EDGARv8 also provides temporal emission profiles for these sectors and for all countries with hourly scaling factors given for weekdays and weekends, as well as scaling factors by day-of-the-week. These scaling factors were applied to the monthly emissions, country-by-country, to produce emission maps for each sector at 3-hourly resolution. These maps were averaged to 0.5° to match the resolution of the modelled transport.

Wildfires

Wildfire emissions were from the Global Fire Assimilation System (GFAS), which assimilated fire radiative power observations from satellites to estimate daily wildfire and biomass burning emissions (Kaiser et al. 2012). The data are provided at 0.1° and were averaged to 0.5° to match the resolution of the modelled transport and interpolated in time to 3-hourly intervals.

Ocean and inland water fluxes

Ocean flux estimates were used from SOCATv2023 which determines sea-air fluxes of CO_2 based on observations of sea-surface pCO_2 and an ocean mixed layer model (Rödenbeck et al. 2013). These estimates are provided at 2.5°×2.0° (longitude × latitude) and at daily temporal resolution and were interpolated to 0.5° and averaged to the state vector time resolution of 28 days. After interpolation, any ocean fluxes that were attributed to a land grid cell at 0.5° were re-attributed to the nearest ocean grid cell and the land cell was set to zero.

Inland water fluxes include a lateral riverine transport of carbon (F_{river}) as well as a lake source of CO_2 (F_{lake}). These estimates were taken from the lateral flux product of Ciais et al. (2020) with a spatial resolution of 5 minutes (0.083°) and annual temporal resolution. The estimates were averaged to 0.5° and interpolated in time to 3-hourly intervals.

This project has received funding from the European Union's Horizon Europe research and innovation programme under grant agreement No 101081395

***Table 1**. Overview of the prior flux estimates with the totals given for Russia for the year 2020. Negative values indicate uptake of CO_2 from the atmosphere.*

Flux component	Data source	Original spatial resolution	Original temporal resolution	Total ($PgCO_2/y$)
F_{fossil}	EDGARv8	0.1°×0.1°	Monthly with day-of-week and hourly profiles	1.86
F_{fire}	GFAS	0.1°×0.1°	Daily	0.66
NEE + F_{LUC}	ORCHIDEE	0.5°×0.5°	3-hourly for NEE and daily for F_{LUC}	-1.13
F_{crop} + F_{wood}	ORCHIDEE	0.5°×0.5°	daily	0.79
F_{lake} + F_{river}	Ciais et al (2021)	0.0833°×0.0833°	annual	-0.28
F_{ocean}	SOCATv2023	2.5°×2.0°	daily	None

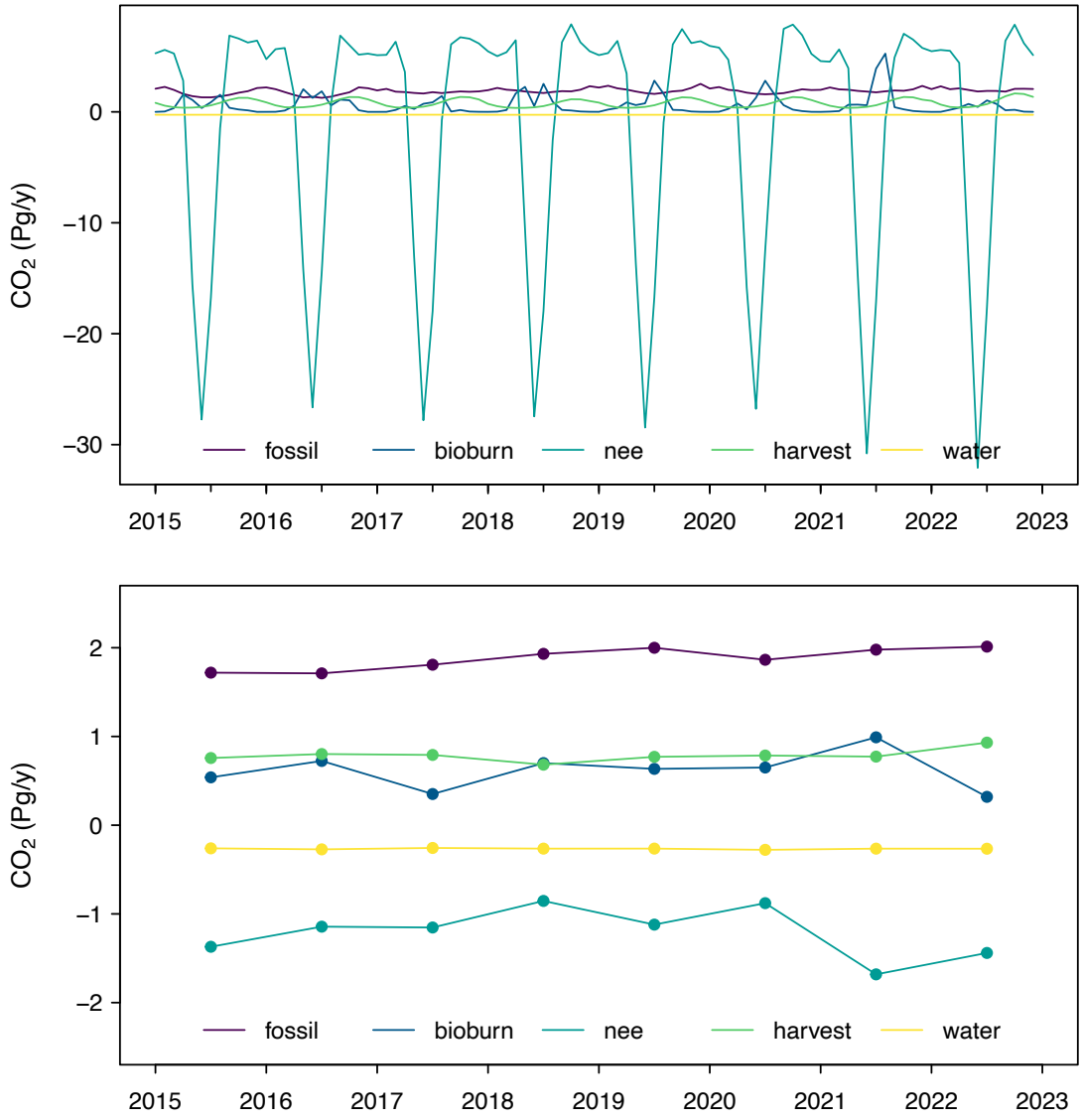

***Figure 2.1.2**. Mean prior source components (REF inversion) for Russia from 2015 to 2022 (units $PgCO_2/y$) shown monthly (top) and annually (bottom).*

This project has received funding from the European Union's Horizon Europe research and innovation programme under grant agreement No 101081395

Prior flux uncertainties and error covariance

The prior uncertainty for the NEE + F_{LUC} flux in each grid cell was calculated as proportional to the mean absolute value in each 6-hourly time step averaged over one year and set to a minimum value of *a* (where *a* is a constant as defined below). To obtain the uncertainty, the mean NEE + F_{LUC} for each 6-hourly time step and grid cell was scaled by a constant, *c*, where:

$$c = a\frac{1}{N}\sum_{i=1}^{N} x_i^{NEE+FLUC} \quad (4)$$

Where *N* is the total number of NEE + F_{LUC} fluxes variables and $x_i^{NEE+FLUC}$ is the flux in each grid cell, and *a* is a reference value for uncertainty ($a = 5\times10^{-5}$ $kgCO_2$ m^{-2} h^{-1}). The resulting uncertainties were used to define the variances and covariances, using correlation that decayed exponentially with distance and time with scale lengths of 200 km and 15 days, respectively. There is no correlation between the 6-hourly flux state variables.

The prior uncertainty for the ocean flux in each grid was calculated as proportional to the mean over all time steps and set to a minimum value of *b* (where *b* is a constant). The uncertainty was obtained by scaling the mean flux in each grid cell by another constant, *d*, where:

$$d = b\frac{1}{N}\sum_{i=1}^{N} x_i^{ocn} \quad (5)$$

where $b = 1\times10^{-6}$ $kgCO_2$ m^{-2} h^{-1}. The resulting uncertainties were used to define the variances and covariances using correlation that decayed exponentially with distance and time with scale lengths of 1000 km and 30 days, respectively. Note that there is no correlation between NEE + F_{LUC} and ocean fluxes.

2.1.3 Atmospheric observations and their uncertainties

Atmospheric observations of CO_2 mole fractions were obtained from the ObsPack product v10.1. The sites used in the inversion were chosen on the basis that they were close to or within the inversion domain and that they had observations covering at least half of the inversion period from 2015 to 2021. The sites, CRP, ICE, MHD, and SIS were also included to help constrain the background mole fraction, which is influenced by fluxes in North America.

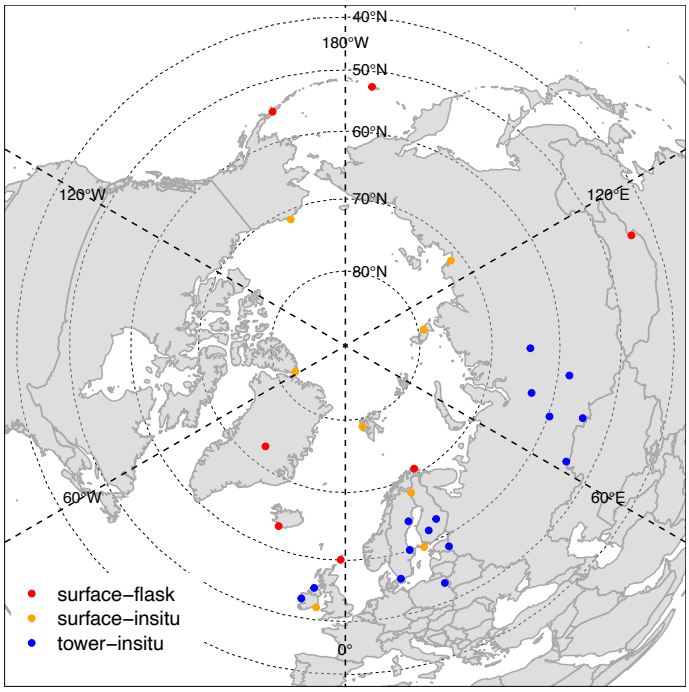

***Figure 2.1.2**. Map of the observation sites*

This project has received funding from the European Union's Horizon Europe research and innovation programme under grant agreement No 101081395

Based on these criteria, 29 sites were used in the inversion of which 22 had in-situ observations and 8 were in Russia (see Figures 2.1.2, 2.1.3 and Table 2.1.1).

***Table 2.1.1**. Atmospheric observation sites used in the inversion*

Site ID	Site Name	Latitude (°N)	Longitude (°E)	Altitude (masl)	Measurement type
ALT	Alert, Canada	82.45	-62.51	195.00	Surface insitu
AZV	Azovo, Russia	54.70	73.03	160.00	Tower insitu
BAR	Baranova, Russia	79.27	101.75	40.00	Surface insitu
BIK	Bialystok, Poland	53.20	22.75	483.00	Tower insitu
BRW	Barrow, Alaska, USA	71.32	-156.61	27.00	Surface insitu
CBA	Cold Bay, Alaska, USA	55.21	-162.72	31.34	Surface flask
CRP	Carnsore Point, Ireland	52.18	-6.37	23.0	Surface insitu
DEM	Demyanskoe, Russia	59.79	70.87	126.00	Tower insitu
HTM	Hyltemossa, Sweden	56.10	13.42	348.40	Tower insitu
ICE	Iceland	64.40	-20.29	123.00	Surface flask
JAR	Järvselja, Estonia	58.28	27.31	146.00	Tower insitu
KJN	Kjolnes, Norway	70.85	29.23	10.00	Surface flask
KRS	Karasevoe, Russia	58.25	82.42	143.00	Tower insitu
MHD	Mace Head, Ireland	53.33	-9.90	29	Tower insitu
NOR	Norunda, Sweden	60.09	17.48	146.00	Tower insitu
NOY	Noyabrsk, Russia	63.43	75.78	151.00	Tower insitu
PAL	Pallas, Finland	67.97	24.12	418.62	Surface insitu
PUI	Puijo, Finland	62.91	27.65	316.00	Tower insitu
SHM	Shemya Isl., Alaska	52.71	174.13	26.00	Surface flask
SIS	Shetland Islands, UK	60.09	-1.26	35.00	Surface flask
SMR	Hyytiala, Finland	61.85	24.29	306.00	Tower insitu
SUM	Summit, Greenland	72.60	-38.42	3214.54	Surface flask
SVB	Svartberget, Sweden	64.26	19.77	385.00	Tower insitu
TIK	Tiksi, Russia	71.60	128.89	29.00	Surface insitu
UTO	Uto, Finland	59.78	21.37	65.00	Surface insitu
UUM	Ulaan Uul, Mongolia	44.45	111.10	1012.00	Surface flask
VGN	Vaganovo, Russia	54.50	62.32	277.00	Tower insitu
ZEP	Zeppelin, Norway	78.91	11.89	279.24	Surface insitu
ZOT	Zottino, Russia	64.48	89.21	415.00	Tower insitu

Observations at continental sites were selected for the daytime 11:00 to 15:00 local time when the PBL is deep minimizing model errors due to misrepresentation of the PBL height. For remote and coastal sites for which there are only flask observations (and the flasks are only filled during “representative conditions”) no time selection was made. There are no mountain sites included and the high altitude sites SUM and UUM are high plateaus.

The uncertainty in the observation space was calculated as the quadratic sum of i) the observation uncertainty and ii) fixed flux influence uncertainty. The first term is calculated based on the standard deviation of the model-observation mismatch using the prior fluxes. The standard deviation did not vary significantly by season for a given site, but did vary significantly for different types of sites, specifically, it was highest at continental sites and lowest at remote and background sites (the observation uncertainty is given in Table 2.1.3). The second term is calculated by propagating the fixed flux uncertainty into the observation space assuming an uncertainty of 50% in the fixed fluxes.

This project has received funding from the European Union’s Horizon Europe research and innovation programme under grant agreement No 101081395

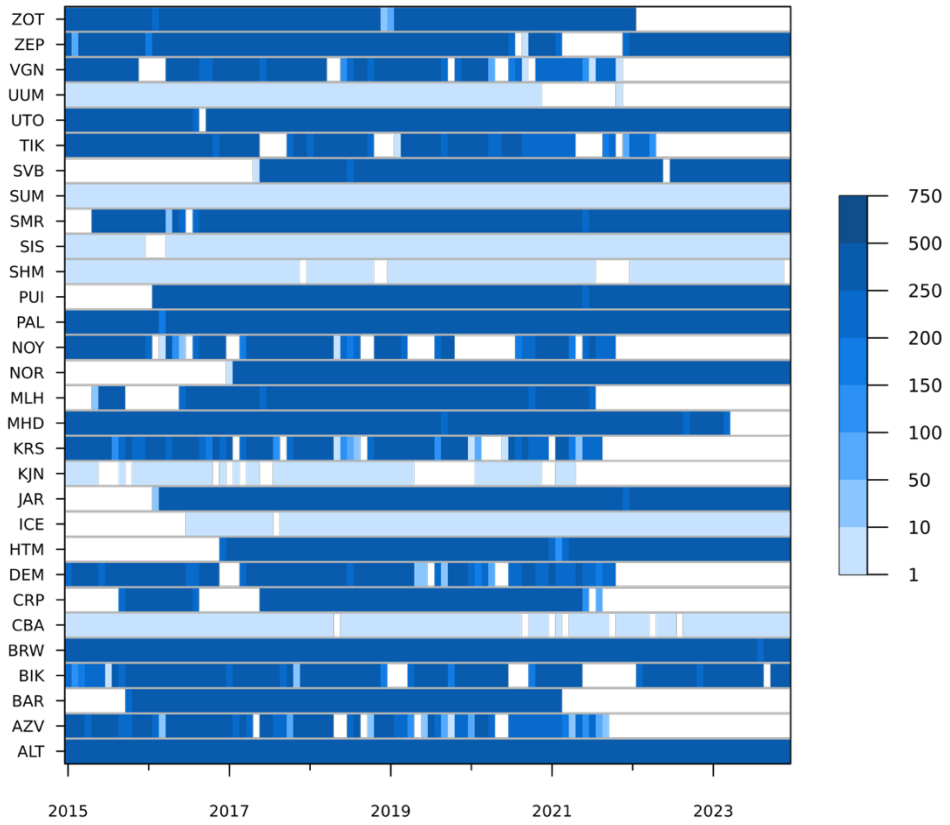

***Figure 2.1.3**. Observation data density by month and site (number of observations per month).*

***Table 2.1.3**. Observation uncertainties used in the inversion*

Site classification	**Sites**	**Observation uncertainty (ppm)**	
		Mar - Aug	**Sep - Feb**
Continental	AZV, BIK, DEM, HTM, JAR, KRS, MLH, NOR, NOY, PAL, PUI, SMR, SWB, UTO, VGN, ZOT	4.7	9.4
Remote	BAR, CRP, KJN, MHD, TIK, UUM	2.0	4.0
Background	ALT, BRW, CBA, ICE, SHM, SIS, SUM, ZEP	1.4	2.8

2.1.4 Sensitivity tests

A number of sensitivity tests were carried out to examine the influence on the posterior NEE+F_{LUC} due to using different prior estimates (see Table 2.1.4). In particular, the sensitivity to the prior NEE+F_{LUC}, harvest fluxes and fossil emissions was tested:

- Test, ORC_adj, uses the crop and wood harvest source from Ciais et al. (2020) directly. However, the NEE flux in ORCHIDEE for the growth of food and biofuel crops, was adjusted to match the crop and wood harvest sink in the Ciais et al. (2020) product. The NEE from ORCHIDEE was adjusted as follows:

$$NEE^{ORC,adj} = NEE^{ORC} + F^{ORC}_{crop+wood}\frac{\left(T^{ORC}_{crop+wood} - T^{Ciais}_{crop+wood}\right)}{T^{ORC}_{crop+wood}}$$

This project has received funding from the European Union's Horizon Europe research and innovation programme under grant agreement No 101081395

where *NEE* is the spatially and temporally resolved flux, *F* is the spatially and temporally resolved NEE flux associated with the crop and wood sink, and *T* is the total area integrated flux for the crop and wood sink.

- Test, ORC_orig, uses the crop and wood harvest fluxes directly from ORCHIDEE, i.e., the source from crop and wood are in the same grid cells as the harvest NEE fluxes. This tests for the sensitivity of the inversion to the spatial distribution of the harvest fluxes.
- Test, REF_noriver, is the same as REF, but excludes the river sink in the fixed flux component. This tests the sensitivity of the inversion to the uncertain river sink term.
- Test REF_fossil is the same as REF, but instead uses the GridFEDv2024 fossil emission estimate.

***Table 2.1.4**. Summary of the sensitivity tests carried out*

Test	**Prior NEE + F_{LUC}**	**Prior F_{CROP} + F_{WOOD}**	**Prior F_{LAKE} + F_{RIVER}**	**Fossil F_{fossil}**
REF	ORCHIDEE	Ciais et al. 2020 scaled to ORCHIDEE F_{CROP} and F_{WOOD}	Ciais et al. 2020	EDGARv8
ORC_adj	ORCHIDEE NEE adjusted	Ciais et al. 2020 F_{CROP} and F_{WOOD}	Ciais et al. 2020	EDGARv8
ORC_orig	ORCHIDEE	ORCHIDEE F_{CROP} and F_{WOOD}	Ciais et al. 2020	EDGARv8
REF_noriver	ORCHIDEE	Ciais et al. 2020 scaled to ORCHIDEE F_{CROP} and F_{WOOD}	Ciais et al. 2020 no river lateral flux	EDGARv8
REF_fossil	ORCHIDEE	Ciais et al. 2020 scaled to ORCHIDEE F_{CROP} and F_{WOOD}	Ciais et al. 2020	GridFEDv2024

2.2 CH_4 inversions

2.2.1. Inversion framework and transport model

We used the global atmospheric inversion model CTE-CH_4 to estimate CH_4 emissions at a 1°×1° resolution over the high northern latitudes and at a weekly temporal resolution using in situ measurements of atmospheric CH_4 mole fractions. The system consists of prior flux maps for different sources, the atmospheric chemistry transport model TM5 (Krol et al., 2005) , and an ensemble Kalman filter data assimilation scheme (Peters et al., 2005) with an ensemble size of 500 and a 5-week lag. TM5 is run at a global horizontal resolution of 3°×2° (latitude × longitude). TM5 is driven by 3-hourly ECMWF ERA5 meteorological data (Hersbach et al., 2020) . Vertically, TM5 has 25 hybrid sigma pressure levels from the surface to the top of the atmosphere. The monthly atmospheric sink due to photochemical reactions with OH based on (Houweling et al., 2014) , which uses the tropospheric OH distribution from (Spivakovsky et al., 2000) multiplied by a factor of 0.92. Cl and O(1D) are based on the atmospheric chemistry general circulation model ECHAM5/MESSy1 (Jöckel et al., 2006) . The inversion model did not account for annual variations in atmospheric sinks and did not optimise the atmospheric sinks.

We simultaneously optimised anthropogenic and natural fluxes at a resolution of 1°×1° over Eurasia from 30N upwards and for Arctic-boreal North America, and regionally elsewhere (see Figure 4). Our prior error covariance matrix **B** is computed as $\mathbf{B} = \mathbf{D}^T \cdot \mathbf{C} \cdot \mathbf{D}$ (Meirink et al., 2008) . For anthropogenic fluxes, the flux uncertainty, **D** is assumed to be 80% of the prior flux over land and 20% of the prior flux over the ocean. For natural fluxes, the flux uncertainty, **D** is assumed to be 100% of the prior flux over land and no optimisation over the ocean. **C** is the correlation matrix that models the correlation as an exponential decay with distance, d between grid cells as $\exp(-d^2/L^2)$. The spatial correlation was defined by an exponential decay (Peters et al., 2005), with a correlation length of 100 km between the 1°×1°

This project has received funding from the European Union's Horizon Europe research and innovation programme under grant agreement No 101081395

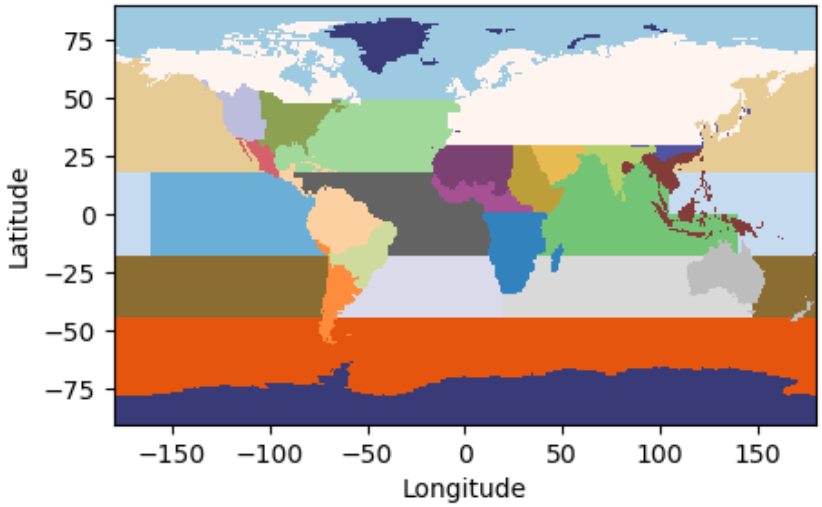

grid-based optimisation domains, 500 km over other land domains and 900 km over ocean domains. The observational uncertainties, diagonal elements of **R**, combine the measurement uncertainty and the model error (model-data-mismatch) in modelling the mixing ratios and ranged from 4.5 to 37.5 ppb for global sites and from 12.5 to 37.5 ppb for Russian sites.

***Figure 2.2.1**. Optimisation regions used for the CH_4 inversions. Fluxes are optimised on 1°×1° grid cells in the white region. The ice regions (dark blue) are not optimised in the inversion.*

2.2.2 Prior fluxes

The prior CH_4 emission estimates were categorized into 8 sectors, summarized in Table 2.2.1: i) Fugitives from fossil fuels (FFF), ii) Combustion (COM), iii) Agriculture and waste (AGW), iv) Wetlands, freshwater, and soil sinks (WET), v) Biomass burning (BBR), vi) Geological (GEO), vii) Termites (TER), and viii) Ocean (OCE). Figure 5 displays the spatial distribution of these fluxes over Russia in 2020. In CTE-CH_4 only biospheric (WET) and anthropogenic sectors are optimised, so the FFF, COM and AGW sectors were combined into one anthropogenic source sector. All other sources were fixed during the inversion. Posterior fluxes for the anthropogenic sectors are split using the flux prior fraction of each of the three sectors in each grid cell.

Anthropogenic emissions

For anthropogenic emissions, prior fluxes were obtained from EDGAR2024 (Crippa et al., 2024) . EDGAR2024 provides data at a spatial resolution of 0.1° × 0.1° and monthly temporal resolution. Within EDGAR2024, the subcategories include:

- Fugitives (FFF): fugitive emissions from fossil fuels.
- Combustion (COM): emissions from the power industry, industrial combustion and processes, buildings and transport.
- Agriculture and waste (AGW): emissions from waste and agriculture.

Anthropogenic prior emissions were converted to 1°×1° spatial resolution and used at monthly temporal resolution in the inversion.

Biospheric emissions

For wetland and soil fluxes, prior estimates were derived from the JSBACH–HIMMELI ecosystem model (deliverable D2.4). This model framework combines JSBACH land ecosystem model with HIMMELI wetland model to simulate peatland, inundated soil, and mineral soil fluxes, and provides wetland and soil CH_4 fluxes at a spatial resolution of 0.5°×0.5° and daily temporal resolution. Additionally, freshwater

This project has received funding from the European Union's Horizon Europe research and innovation programme under grant agreement No 101081395

fluxes were included following (Johnson et al., 2022) for lakes and (Rocher-Ros et al., 2023) for rivers, with global lake and river totals scaled to 13 Tg yr^{-1} and 12 Tg yr^{-1}, respectively, consistent with the lower-limit estimate of the Global Methane Budget (Saunois et al., 2025). The freshwater fluxes were originally at a spatial resolution of 0.25°×0.25° and temporal resolutions of daily (lakes) and monthly (rivers). The combined prior biospheric emissions were used at daily resolution, with the monthly river emissions padded to daily. All biospheric prior emissions were converted to 1°×1° spatial resolution.

Other emissions sources

Biomass burning (BBR) emissions were taken from GFAS (Kaiser et al., 2012) , covering emissions from open biomass burning, and were used at daily resolution in the inversions and converted to 1°×1° spatial resolution. Geological fluxes (GEO) were taken from (Etiope et al., 2019) representing onshore geological sources, and scaled globally to 15 Tg yr^{-1} following Saunois et al. (2025). Ocean emissions (OCE) were based on the climatological dataset of (Weber et al., 2019) , which accounts for both diffusive and ebullitive fluxes. Finally, termite emissions (TER) were prescribed from Saunois et al. (2025). Geological, ocean and termite emissions were originally at a spatial resolution of 1°×1° and monthly temporal resolution.

Table 2.2.1. *CH_4 prior fluxes used in the inversion.*

Category Abb.	**Source Sector**	**Data source**	**Temporal resolution**	**Time period**
FFF	Fugitives from fossil fuels	EDGARv2024	monthly	2005-2023
COM	Combustion	EDGARv2024	monthly	2005-2023
AGW	Agriculture and waste	EDGARv2024	monthly	2005-2023
WET	Wetlands and soil sinks	JSBACH-HIMMELI Global	daily	2005-2023
WET	Freshwater	Johnson et al., 2022†	daily	Climatology
WET	Freshwater	Rocher-Ros et al., 2023‡	monthly	Climatology
BBR	Biomass burning	GFASv1.2	daily	2005-2023
GEO	Geological	Etiope et al., 2019*	monthly	Climatology
TER	Termites	Castaldi, 2013	monthly	Climatology
OCE	Ocean	Weber et al., 2019	monthly	Climatology

†Small lakes (<0.1 km^2) are unscaled, large lakes (>5000 km^2) are scaled down to 10% of the fluxes in Johnson et al. (2022). All remaining lakes are scaled such that the global yearly total from lakes is 13 Tg/yr, the lower limit in Saunois et al., (2025).

‡Global total scaled down to 12 Tg/yr, the lower limit in Saunois et al., (2025).

*Global total scaled down to 15 Tg/yr, and excluding ocean fluxes (Petrenko, et al. (2017)).

This project has received funding from the European Union's Horizon Europe research and innovation programme under grant agreement No 101081395

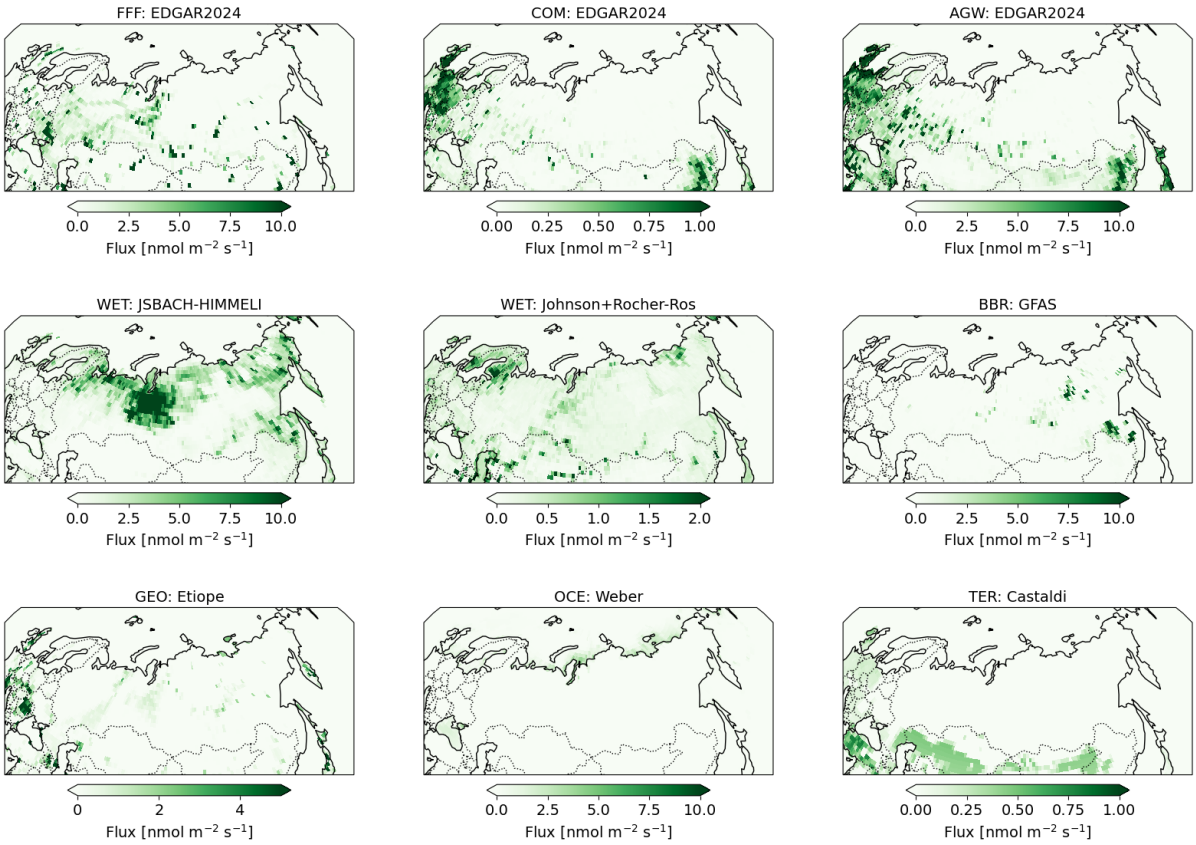

Figure 2.2.2. *Average prior methane emissions by source for 2020 at a spatial resolution of 1°×1°. Note that the colour scales of the maps vary.*

2.2.3 Atmospheric observations and their uncertainties

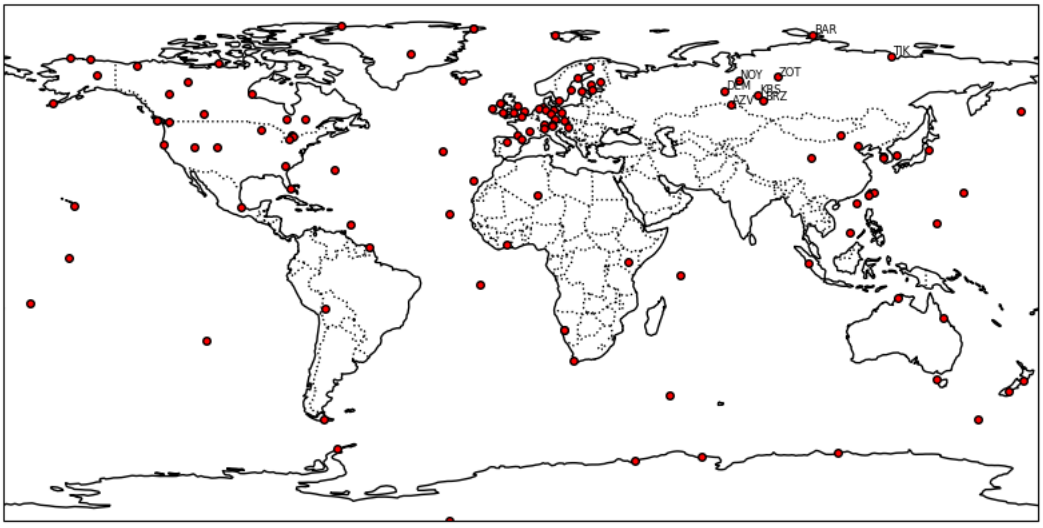

Figure 2.2.3. *Location of sites used in the CH_4 inversions. Site labels are included for the Russian sites.*

This project has received funding from the European Union's Horizon Europe research and innovation programme under grant agreement No 101081395

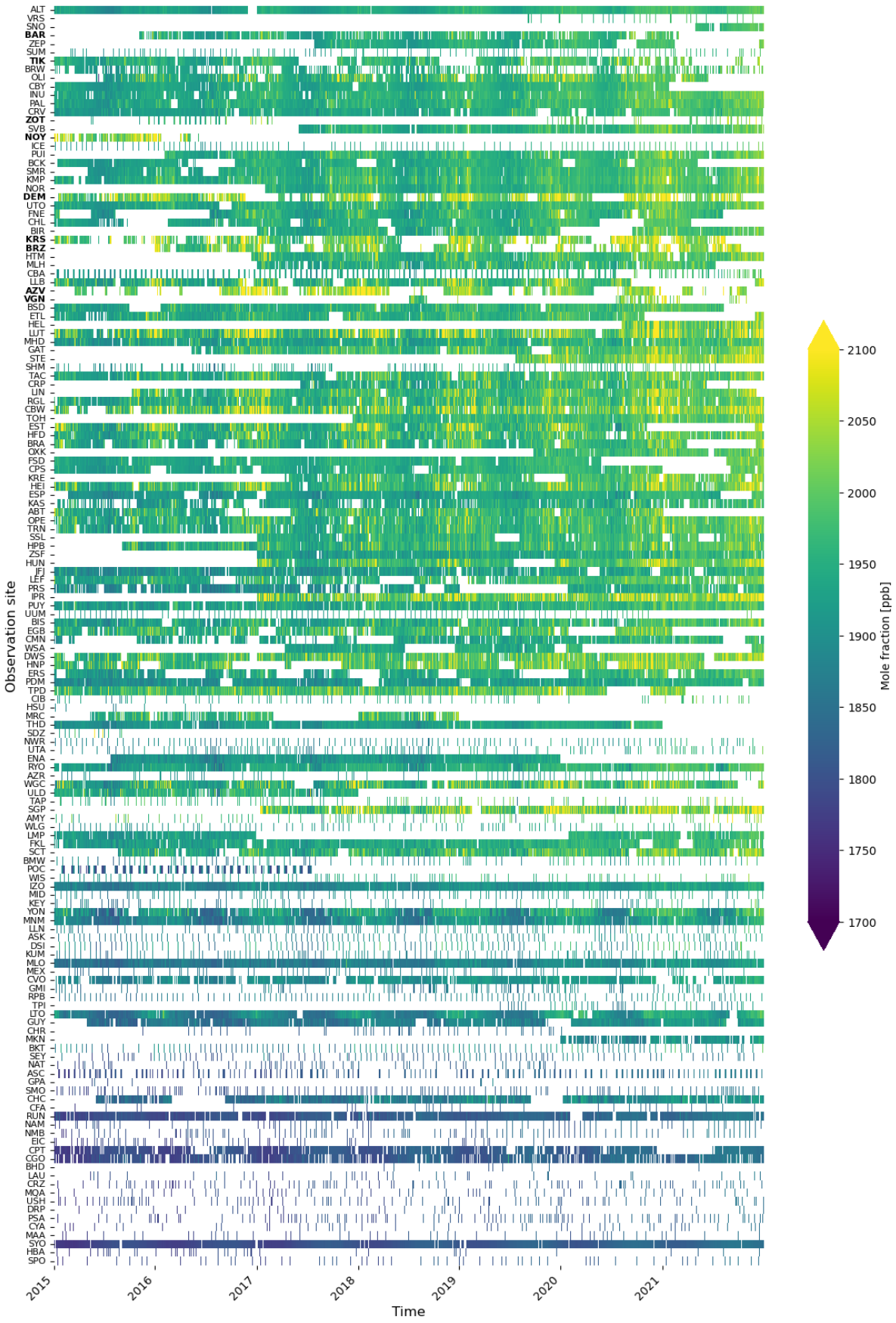

Figure 2.2.4. *Observation temporal coverage in latitudinal order. Russian sites are shown in* ***bold****.*

This project has received funding from the European Union's Horizon Europe research and innovation programme under grant agreement No 101081395

We used observations from a global in situ measurement network, ICOS Obspack v10.0 (Bergamaschi et al., 2024), NOAA Obspack v7.0 (Schuldt et al., 2024) and the National Institute for Environmental Studies, Japan (NIES) (Sasakawa et al., 2010) . The data included weekly discrete air samples as well as hourly continuous measurements. The data were filtered according to the quality flags of the data providers. Only data points representing well-mixed conditions were used: the hourly continuous observations were pre-processed to daily averages by averaging from 12 to 4 pm local time, except for the high mountain sites, from which averages were taken from 0 to 4 am local time, similar to (Tsuruta et al., 2017) . Observational uncertainty, also known as model-data mismatch, was defined for each site based on site characteristics and measurement accuracy adapted from previous studies (Bruhwiler et al., 2014; Tenkanen et al., 2024; Tsuruta et al., 2017, 2019) and reflected the ability of the model to predict atmospheric concentrations. In Russia, there were 9 sites (locations in Fig. 2.2.3 and observations in Fig. 2.2.4) and globally 118 stations across 2015-2021.

3. Results

3.1 CO_2 inversions

3.1.1. Comparison of modelled and observed atmospheric CO_2 mole fractions

Figure 3.1.1 shows the comparison of CO_2 mole fractions from the observations versus those simulated using the prior and posterior fluxes for the reference inversion and at selected representative sites for the year 2015. The prior fluxes underestimate CO_2 mole fractions at all sites in the autumn and winter months at continental sites and for all years, which may be due to an underestimate of the fixed flux component, principally fossil and harvest emissions, and/or the ecosystem respiration flux. On the other hand, the prior fluxes lead to an overestimate of the mole fractions in summer months, which may be due to an underestimate of NEE uptake and/or an overestimate of fixed fluxes for this period. The posterior fluxes improve the fit to the observed mole fractions but still tend to underestimate the observations in autumn and winter and overestimate them in summer.

An assessment of the agreement of the modelled to the observed mole fractions is given using the statistics of the Normalized Standard Deviation (NSD) and correlation coefficient (R) and is presented in Figure 3.1.2 for all sites and for the example year, 2015. The correlation of the observations with the modelled mole fractions using the posterior fluxes improves at all sites, while the NSD becomes closer to one at most sites, indicating an overall improvement of the agreement with the observations. The correlation with modelled mole fractions using the prior fluxes is already quite strong at all sites, i.e., > 0.7 and increases further when using the posterior fluxes, for which it is generally > 0.8.

3.1.2. Monthly and annual NEE + F_{LUC} fluxes

Figure 3.1.3 shows the monthly and annual mean NEE + F_{LUC} fluxes integrated over Russia from 2015 to 2021. In all years, the posterior NEE + F_{LUC} is less negative (indicating less uptake) than the prior estimates. Averaged over all years, the sink in the reference inversion decreases from -1.21 $PgCO_2$/y (-0.33 PgC/y) a priori to -0.75 $PgCO_2$/y (-0.204 PgC/y) a posteriori. This difference is due to an increase in the positive flux during autumn and winter months, i.e., from September to January, while the summer uptake is, at the scale of Russia, largely unchanged. Overall, the seasonality of the posterior NEE + F_{LUC} is very similar to that of the prior.

The inter-annual variability in the posterior NEE + F_{LUC} is also similar to that in the prior with a pronounced increase in uptake in 2020 and 2021 compared to the other years.

This project has received funding from the European Union's Horizon Europe research and innovation programme under grant agreement No 101081395

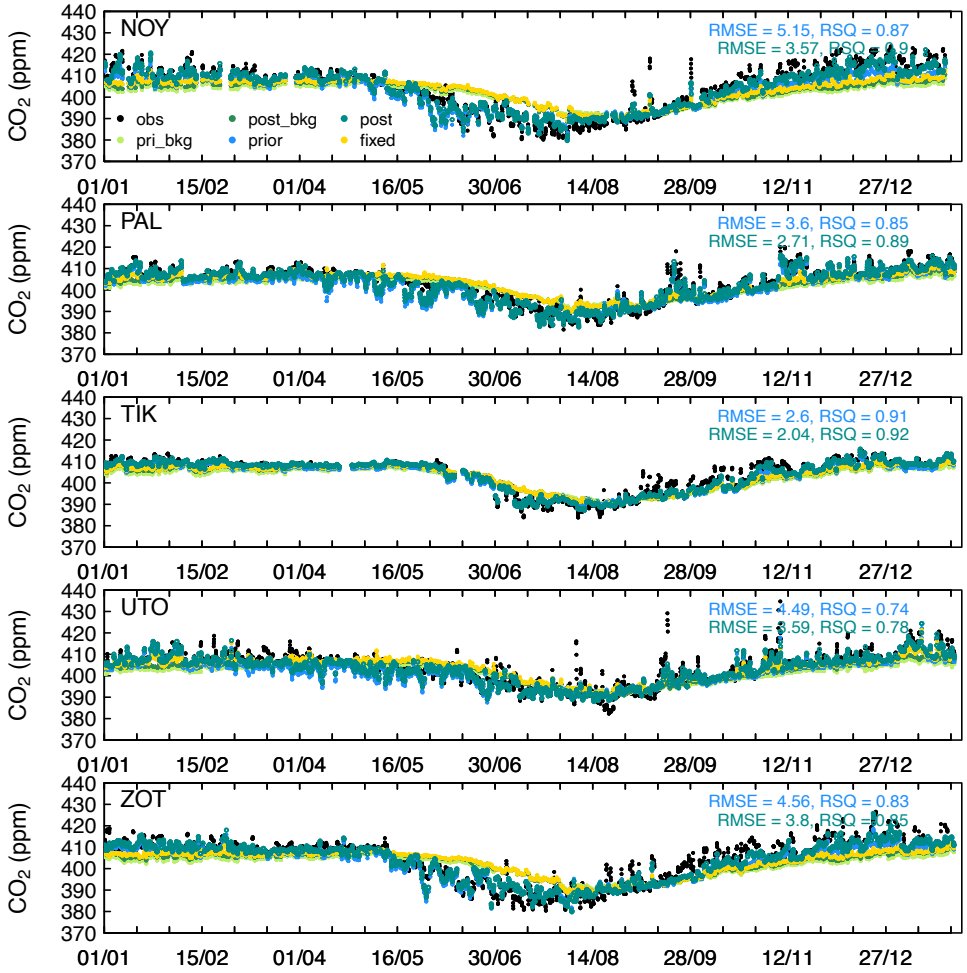

Figure 3.1.1. *Observed, prior and posterior CO_2 mole fractions for example sites and the year 2015.*

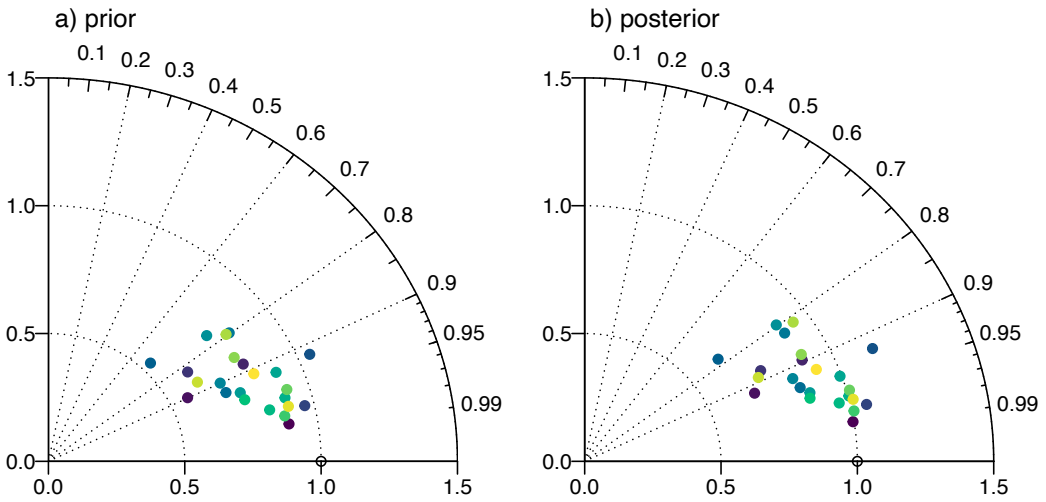

Figure 3.1.2. *Taylor diagrams comparing the agreement between a) the prior and observed versus b) the posterior and observed CO_2 mole fractions for all sites and the year 2015.*

This project has received funding from the European Union's Horizon Europe research and innovation programme under grant agreement No 101081395

***Table 3.1.1**. Annual total NEE + F_{LUC} fluxes for Russia from the different sensitivity tests for the year 2015.*

Test	Prior NEE + F_{LUC} ($PgCO_2/y$)	Posterior NEE + F_{LUC} ($PgCO_2/y$)
REF	-1.37	-0.78
ORC_adj	-1.23	-0.64
ORC_orig	-1.37	-0.79
REF_noriver	-1.37	-0.81
REF_fossil	-1.37	-0.76

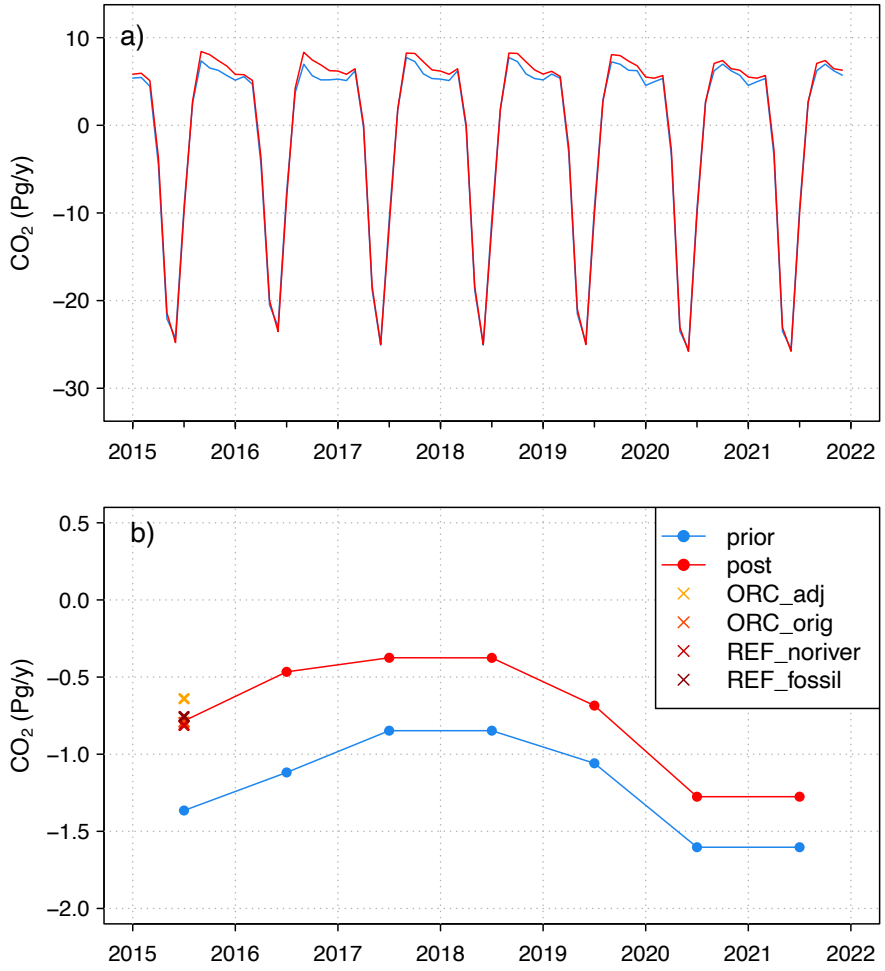

***Figure 3.1.3**. Monthly and annual mean prior and posterior NEE + F_{LUC} integrated over Russia from 2015 to 2021 (units $PgCO_2/y$). Also shown are the annual totals for 2015 for the sensitivity tests.*

The results of the sensitivity tests run for the year 2015 are summarized in Table 3.1.1. The test using the crop and wood harvest fluxes from Ciais et al. (2020) with the adjusted NEE (ORC_adj) has the smallest prior and posterior carbon sink (-0.64 $PgCO_2/y$). On the other hand, changing simply the distribution of the harvest fluxes, i.e. the difference between the test ORC_orig versus REF, makes little difference to the results. The test omitting the very uncertain river sink term in the fixed flux component (REF_noriver), results in a slightly larger carbon sink (-0.81 $PgCO_2/y$). While the test using the GridFED fossil emissions (REF_fossil) results in a slightly smaller carbon sink than the REF inversion (-0.76 $PgCO_2/y$) despite the GridFED emissions being larger than those from EDGARv8 by 0.3 $PgCO_2/y$. This apparent discrepancy is explained by the fact that the sparse observations that are remote from built-up areas are not very sensitive to the change in fossil emissions. Moreover, there may be an influence of the temporal variability of the emissions – the EDGARv8 emissions were calculated hourly while the GridFED emissions are only monthly.

This project has received funding from the European Union's Horizon Europe research and innovation programme under grant agreement No 101081395

Since the NEE calculated in ORCHIDEE includes that for the growth of crop and wood, which are harvested, the source associated with their consumption or combustion needs to be subtracted from the NEE to obtain the net LULUCF flux for Russia. However, only the source from crop and wood harvested in Russia should be added, i.e., the source excluding crop and wood imported, but including that exported. In the inversions REF and ORC_orig, this was taken to be equivalent to the NEE associated with crop and wood harvest, which is equivalent to the crop and wood source. However, for the inversion ORC_adj, this was taken to be equivalent to the crop and wood sink in the product of Ciais et al. (2020).

The ORCHIDEE crop and wood harvest flux averaged over 2015 – 2021 is 0.77 $PgCO_2/y$. After correction for this term the Russian land biosphere is nearly carbon neutral, with NEE + F_{LUC} + $F_{crop+wood}$ of 0.02 $PgCO_2/y$ for this time period in the REF inversion, and only in 2020 and 2021 is the land biosphere a carbon sink of -0.50 $PgCO_2/y$. The Ciais et al. (2020) crop and wood harvest sink in 2015 is 0.43 $PgCO_2/y$. After adjusting the inversion ORC_adj for the crop and wood harvest, the total sink is -0.21 $PgCO_2/y$. Thus, depending on the harvest source, the Russian land biosphere could be a small sink or nearly carbon neutral.

3.1.3. Spatial distribution of NEE + F_{LUC} fluxes

In the prior estimates, the NEE + F_{LUC} CO_2 uptake is mostly located in western and southern Russia. The inversion, however, consistently reduces the uptake in western Russia and particularly in western Siberia, that is, these areas have positive flux increments (Fig. 3.1.4). In the posterior NEE + F_{LUC}, CO_2 uptake becomes largely limited to the area of southwestern Russia in most years, except 2020 and 2021 when uptake is seen across western Russia. On the other hand, from 2016 to 2018, the land biosphere of western Russia is a small source of CO_2.

3.1.4. Posterior uncertainty and uncertainty reduction

The posterior uncertainty related to the constraint of the observations, was estimated using a Monte Carlo ensemble. The members of the ensemble were generated by adding random Gaussian distributed errors to the prior fluxes (consistent with the error statistics of the **B** matrix) and to the observations (consistent with the error statistics of the **R** matrix). The posterior uncertainty was calculated from the distribution of the posterior fluxes from the ensemble, and the uncertainty reduction was determined as one minus the ratio of the posterior to prior uncertainties (Figure 3.1.5). The uncertainty reduction was overall quite weak, with large expanses of Russia with close to no uncertainty reduction. The best constrained regions were central Siberia and northeastern Siberia, where the uncertainty reduction reached around 20%. The spatial pattern of the uncertainty reduction is, as expected, strongly correlated with the location of the observation sites and thus the observation constrain. For the total annual NEE + F_{LUC} for Russia the prior uncertainty was 0.14 $PgCO_2/y$ and the posterior uncertainty was 0.13 $PgCO_2/y$ indicating only a very minor reduction in the overall uncertainty.

This project has received funding from the European Union's Horizon Europe research and innovation programme under grant agreement No 101081395

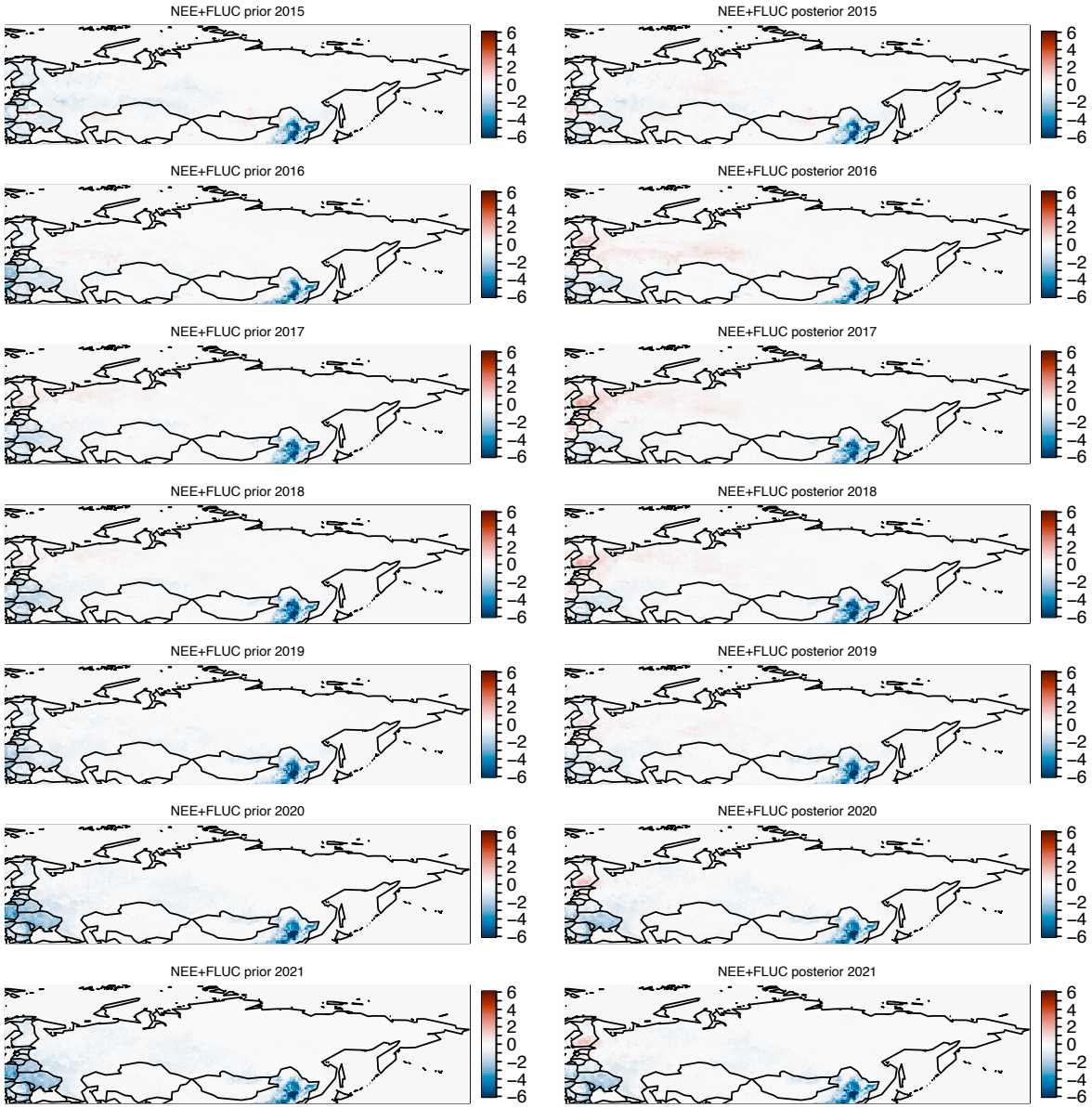

Figure 3.1.4. *Maps of the prior and posterior NEE + F_{LUC} fluxes for years 2015 to 2021 for the reference inversion.*

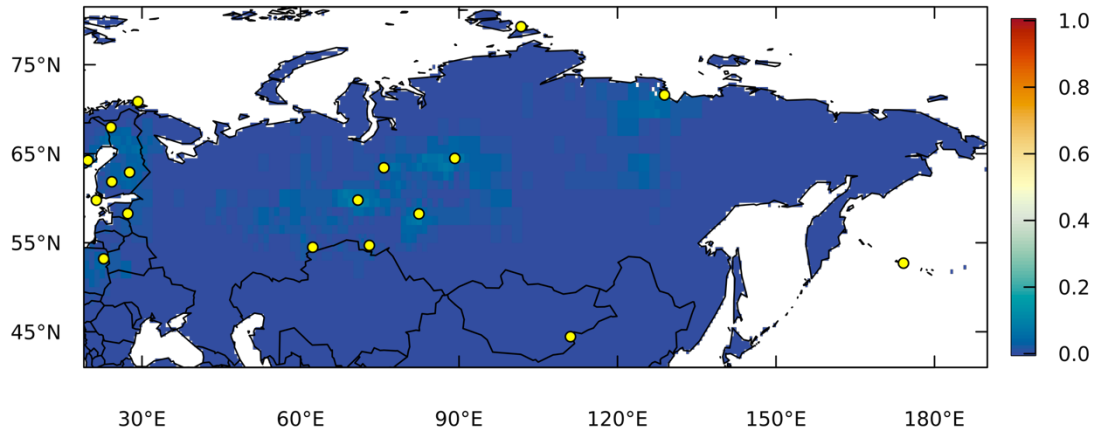

Figure 3.1.5. *Uncertainty reduction in the annual mean NEE + F_{LUC} fluxes for the year 2015. The yellow dots indicate the locations of the atmospheric observation sites.*

This project has received funding from the European Union's Horizon Europe research and innovation programme under grant agreement No 101081395

3.2 CH_4 inversions

3.2.1 Comparison of modelled and observed atmospheric CH_4 mole fractions

We compared the observed CH_4 mole fractions used in the inversion with the modelled mole fractions before and after optimisation. We calculated the linear correlation coefficient (R), coefficient of determination (R^2), root mean square error (RMSE), and bias between the observed and modelled values. The statistics for the Russian sites are depicted in Fig. 3.2.1. From the prior to the posterior, there is a reduction in RMSE across all Russian sites. A pronounced negative bias is evident in the prior, which becomes less negative or slightly positive in the posteriors. Additionally, the correlation increases from the prior to the posterior. These statistics indicate an enhanced fit to the observations after optimisation. Table 3.2.1 presents the average statistics for all sites in the inversion and the Russian sites separately. The bias and RMSE suggest that the priors align more closely with the data globally than with the Russian sites, although the correlation is lower. The relative difference values between the prior and posterior demonstrate that the global average exhibits a greater improvement in fit after optimisation compared to the Russian subset. Overall, these results confirm that the inversion reduces discrepancies between the model and observations by decreasing the bias and RMSE while enhancing the correlation with the observations.

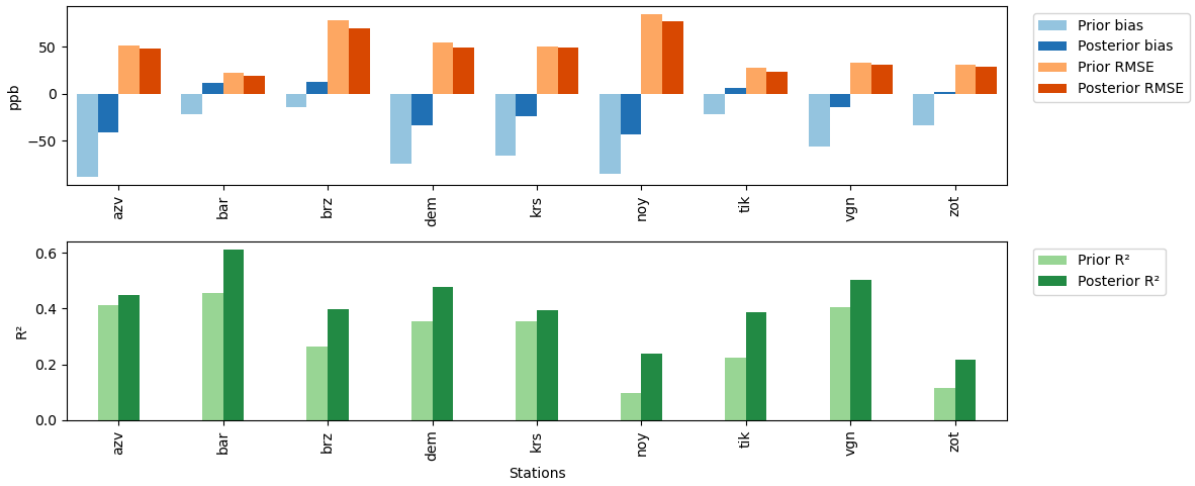

Figure 3.2.1. *Overview of statistical results for assimilated observed mole fractions and CTE-CH_4 posterior and prior simulated concentrations for sites in Russia used in the inversion: RMSE and bias (upper panel), and correlation (lower panel).*

All sites	**Prior**	**Posterior**	**Relative difference**
Bias (ppb)	-33.7	0.8	-1.03
RMSE (ppb)	39.8	34.6	-0.13
R^2	0.21	0.35	0.68
Russian sites	**Prior**	**Posterior**	**Relative difference**
Bias (ppb)	-43.8	-8.1	-0.82
RMSE (ppb)	47.4	42.3	-0.11
R^2	0.26	0.39	0.47

Table 3.2.1. *Statistics on the performance of the CTE-CH_4 compared to assimilated mole fraction measurements, before (prior) and after (posterior) the inversions for all the sites assimilated (top table) and for the Russian sites (bottom table). The bias, root mean square error (RMSE) and coefficient of determination (R^2) values for the mean prior, posterior and relative difference (RDiff).*

This project has received funding from the European Union's Horizon Europe research and innovation programme under grant agreement No 101081395

3.2.3 Annual and monthly emission estimates

Table 3.2.3 presents the average annual CH_4 emissions for Russia across each sector from 2015 to 2021. For the optimised sectors, the prior, posterior, and percentage change in emissions are documented. The total emissions from all sectors indicate a modest increase of 2.8%, with variations observed across individual sectors. Notably, the AGW and COM sectors exhibit larger increases in emissions, at 9.0% and 7.8%, respectively, while the WET and FFF sectors demonstrate smaller increases of 1.9% and 2.2%, respectively. A reduction in uncertainties is observed from prior to posterior estimates across all sectors.

Sector	Prior (Tg yr^{-1})	Posterior (Tg yr^{-1})	% Change
AGW	6.73 ± 0.51	7.34 ± 0.45	+9.0%
WET	23.83 ± 0.57	24.29 ± 0.49	+1.9%
COM	0.19 ± 0.01	0.20 ± 0.01	+7.8%
FFF	8.95 ± 1.15	9.15 ± 0.94	+2.2%
BBR	3.14	–	–
GEO	1.06	–	–
OCE	1.66	–	–
TER	0.05	–	–
Total	**45.61 ± 1.44**	**46.88 ± 1.20**	**+2.8%**

Table 3.2.3. *Average annual CH_4 emissions for Russia for each optimised sector for the period 2015-2021. For optimised sectors the prior, posterior and percentage change are included. For non-optimised sectors, only the prior emissions are included.*

Seasonal variations, depicted in monthly time series in Figure 3.2.2 and Figure 3.2.3 (excluding WET and total emissions to highlight variations in smaller sectors), reveal that the WET sector predominantly influences posterior total emissions outside the winter months. Emissions from the WET sector are minimal during winter, peaking in July annually. In certain years, such as 2015, 2020, and 2021, the peak in WET emissions surpasses prior estimates, while in other years, it remains equal or lower. The BBR sector also contributes to seasonality of the total emissions, with one or two peaks annually, occurring between April and October, although emissions are considerably lower than those of the WET sector. The FFF and AGW sectors exhibit fluctuations from prior estimates, typically peaking in winter months, in contrast to the minimal month-to-month variations observed in prior estimates.

This project has received funding from the European Union's Horizon Europe research and innovation programme under grant agreement No 101081395

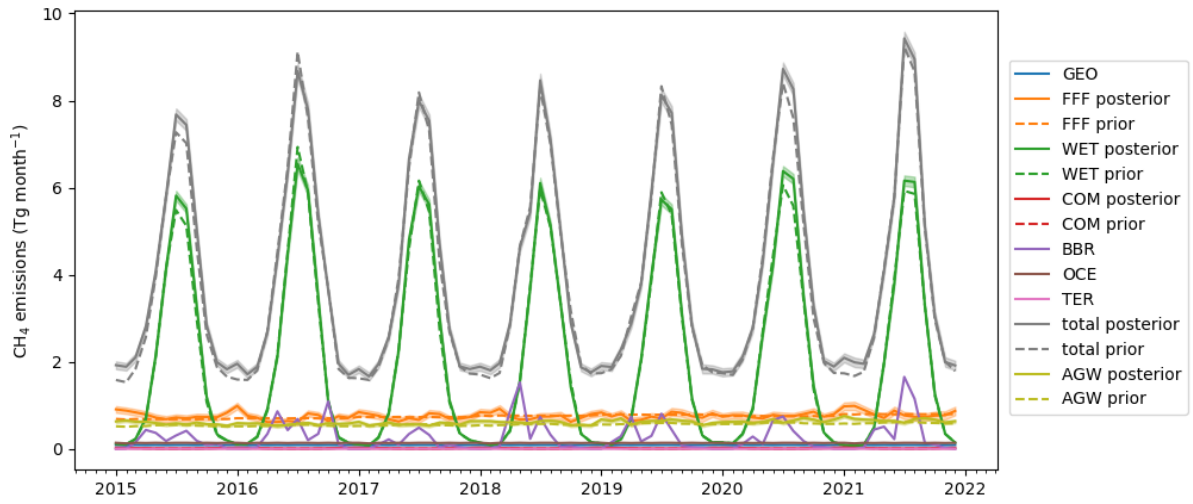

Figure 3.2.2. *Time series of monthly CH_4 emissions for Russia showing total and sectoral contributions for the period 2015-2021. Posterior fluxes are shown as solid lines and prior fluxes as dashed lines. Sectors that are not optimised are shown without uncertainties.*

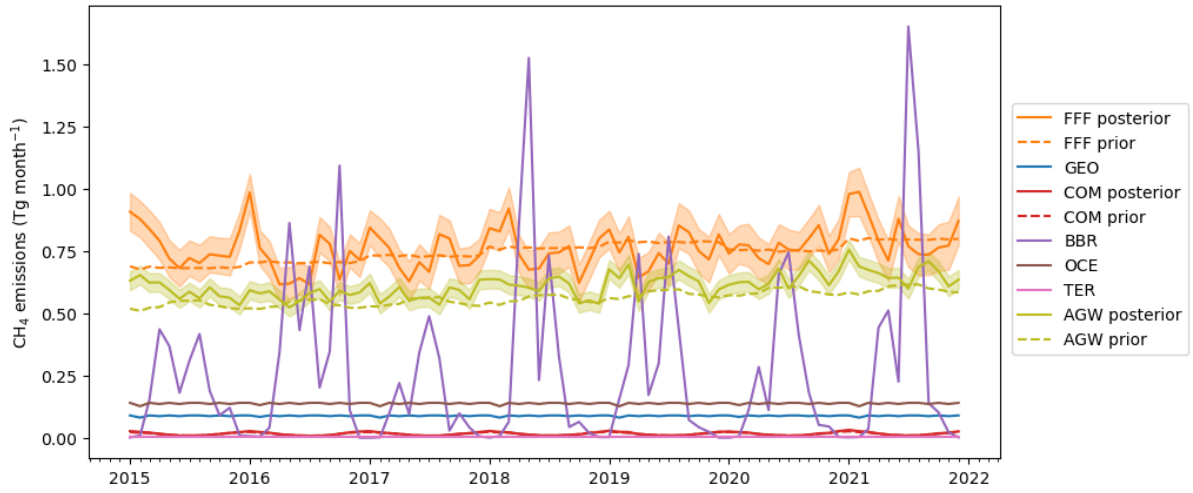

Figure 3.2.3. *Same as Figure 16, but without the WET sector and totals. Time series of monthly CH_4 emissions for Russia showing sectoral contributions for the period 2015-2021. Posterior fluxes are shown as solid lines and prior fluxes as dashed lines. Sectors that are not optimised are shown without uncertainties.*

3.2.3 Spatial distribution of prior and posterior emissions

Despite small changes in the total emissions from all of Russia from the prior to the posterior, the spatial distributions reveal substantial regional variations. The average spatial distribution across the 2015-2021 period of the prior and posterior emissions and their difference (posterior minus prior) are shown in Figure 3.2.4 for the sectors optimised in the inversion (WET, AGW, FFF and COM) and for the total emissions.

For the WET sector, a decrease in emissions from the prior to the posterior is observed in Russian Karelia and Murmansk, the northern part of the West Siberian Lowlands (WSL), the Taymyr Peninsula and the northern far east of Russia. An increase in emissions was observed in northwestern Russia, the central and southern WSL, and the southern far east of Russia, with the WSL showing the largest

This project has received funding from the European Union's Horizon Europe research and innovation programme under grant agreement No 101081395

increase in emissions. In much of central Siberia, there was no little change from the prior to the posterior, where there were no observations to constrain the inversion.

Emissions from the COM and AGW sectors are predominantly concentrated in southwestern and south-central Russia, with minimal emissions detected in the northern and eastern regions. FFF emissions were also present in these areas but were more widespread, with substantial emissions in the West Siberian Lowlands and notable hotspots in the East. Changes in emissions from prior to posterior are consistent across the anthropogenic sectors, as they are optimised together in the inversion. Therefore, where sources overlap, the pattern appears similar. In southwestern and central Russia, emissions from anthropogenic sectors overall increased from the prior to the posterior. The FFF sector exhibited high emissions in the West Siberian Lowlands, which also increased from the prior. In the East, where FFF emission hotspots are located, most of these decreased from the prior, with a few exceptions showing an increase. A significant decrease in FFF emissions was observed over a hotspot in south-central Russia.

The overall spatial pattern of total emissions (encompassing all sectors, including those not optimised) is characterised by dominance of the WET sector in northern Russia and the anthropogenic sectors in southern Russia.

This project has received funding from the European Union's Horizon Europe research and innovation programme under grant agreement No 101081395

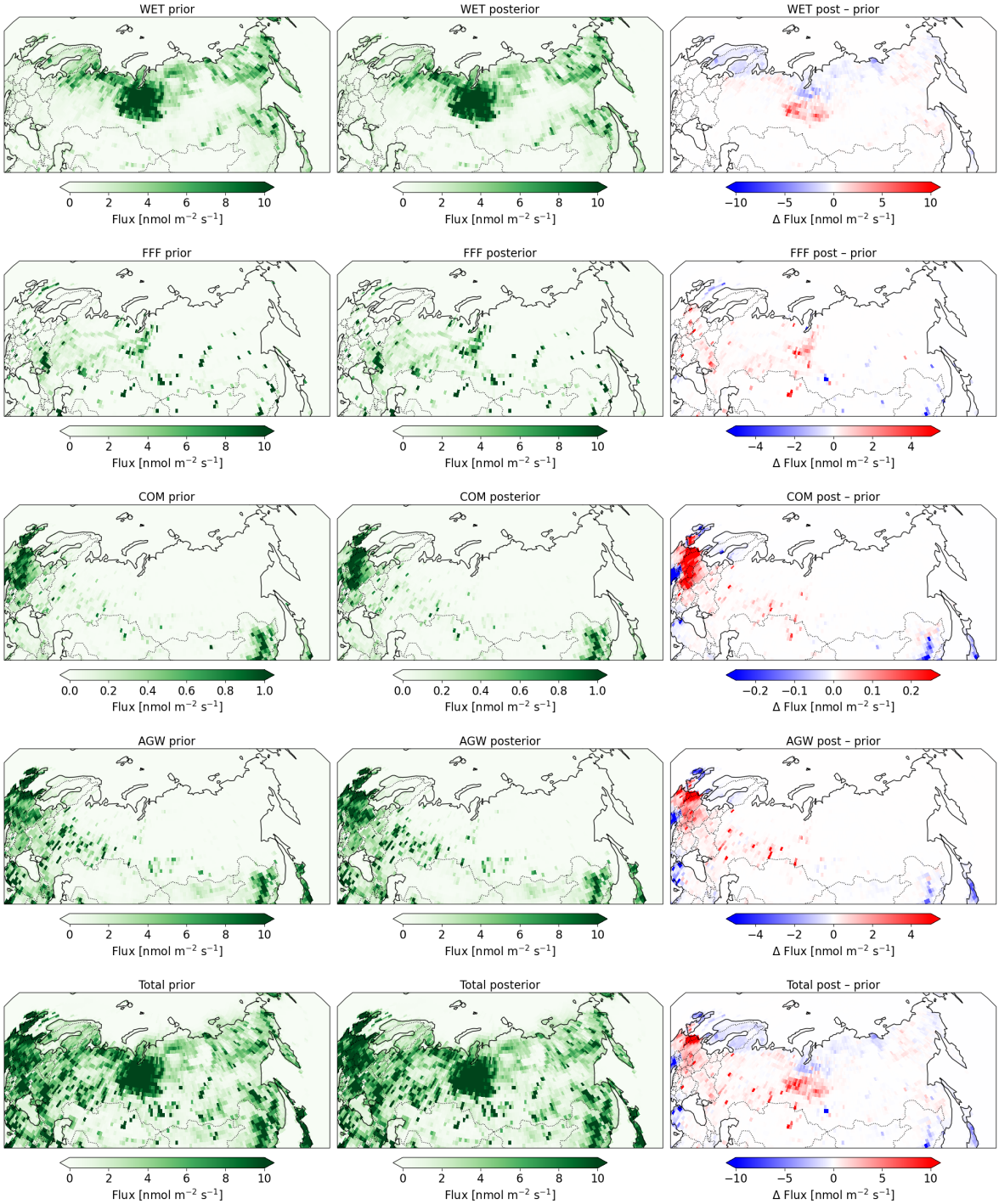

Figure 3.2.4: *Mean spatial distribution of CH_4 fluxes from the CTE-CH_4 inversion (2015–2021) at 1° × 1° resolution for the four optimised sectors (top four rows) and total emissions (bottom row). Shown are prior (left), posterior (middle), and posterior–prior increments (right). Note that the colour scales of the maps vary.*

4. Deviations from the description of action

The inversions of CO_2 and CH_4 for Russia were run for the period 2015 to 2021, instead of the for the full period originally planned, which was up to and including the year 2023. This is because the observations from the network of tall towers across Russia, i.e., JR-STATION, are presently only available up to the end of 2021. If more recent observations become available during the final year of EYE-CLIMA, the CO_2 and CH_4 inversions will be extended to include the new data.

This project has received funding from the European Union's Horizon Europe research and innovation programme under grant agreement No 101081395

5. Conclusions

The inversions for NEE + F_{LUC} fluxes resulted in an improved fit of the modelled versus the observed CO_2 mole fractions, increasing the correlation and reducing the RMSE. Integrated over Russia, the posterior NEE + F_{LUC} was less negative than the prior for all years, indicating a weaker carbon sink. Averaged over all years, the sink decreased from -1.21 ± 0.14 $PgCO_2/y$ (-0.33 PgC/y) a priori to -0.75 ± 0.13 $PgCO_2/y$ (-0.204 PgC/y) a posteriori. This difference is due to an increase in the positive flux during autumn and winter months, i.e., from September to January, while the summer uptake is, at the scale of Russia, largely unchanged. Sensitivity tests were carried out for the year 2015 to examine the sensitivity of the results to different prior NEE as well as fixed harvest flux and fossil fuel emission estimates. The range in posterior NEE + F_{LUC} in 2015 across all sensitivity tests was -0.81 to -0.64 $PgCO_2/y$. After correcting the posterior NEE + F_{LUC} for the harvest NEE, of 0.77 $PgCO_2/y$, the Russian land biosphere is nearly carbon neutral, with NEE + F_{LUC} + $F_{crop+wood}$ of 0.02 $PgCO_2/y$ averaged over 2015 to 2021, and only in 2020 and 2021 is the land biosphere a carbon sink of -0.50 $PgCO_2/y$. However, this result is quite uncertain owing to the uncertainties in the fossil emissions and the harvest fluxes.

For CH_4, the posterior modelled mole fractions demonstrate an improved fit to the observations compared to the prior. Across the Russian sites, RMSE decreases, correlations increase, and the strongly negative prior bias becomes less negative or slightly positive after optimisation. When averaged across all sites, both globally and within Russia, reductions in RMSE and bias confirm the improved model–observation fit, although the global average exhibits a larger overall improvement than the Russian subset. Posterior CH_4 emissions for Russia show only a modest increase in total fluxes from 2015–2021 (2.8%), yet this masks sectoral differences – agriculture plus waste and combustion emissions increase more substantially (by 9.0% and 7.8%, respectively), while increases in wetland and freshwater and fugitive fossil fuel emissions are smaller. Monthly emissions show a pronounced seasonal cycle dominated by wetland fluxes, with an annual peak in July. Smaller but important contributions are shown from the biomass burning sector and winter peaks in the anthropogenic sectors. Spatially, wetland emissions remain the principal source in northern Russia, while anthropogenic sources dominate the south. Posterior adjustments show strong regional redistribution, including decreased wetland and freshwater emissions in Karelia and Murmansk, northern West Siberian Lowlands, the Taymyr Peninsula, and the northern Far East, contrasted with increases in the central and southern West Siberian Lowlands and parts of the Far East. Anthropogenic sectors show increases across southwestern and central Russia, as well as and the West Siberian Lowlands, but varying adjustments over eastern hotspot regions. Overall, the inversion reduces model–observation discrepancies and shows distinct seasonal and spatial patterns in Russian CH_4 emissions.

This project has received funding from the European Union's Horizon Europe research and innovation programme under grant agreement No 101081395

6. References

Bakels, L., Tatsii, D., Tipka, A., Dütsch, M., Blaschek, M., Bucci, S., Plach, A., Vojta, M., Seibert, P., Pisso, I., Eckhardt, S., Cassiani, M., Zwaaftink, C. G., Mulder, M., and Stohl, A.: FLEXPART-11: Advancements in a Lagrangian Atmospheric Model for Enhanced Accuracy, Efficiency, and Flexibility, https://doi.org/10.5194/egusphere-egu24-2652, 2024.

Berner, R. A. and Caldeira, K.: The need for mass balance and feedback in the geochemical carbon cycle, Geology, 25, 955–956, https://doi.org/10.1130/0091-7613(1997)025<0955:tnfmba>2.3.co;2, 1997.

Bintanja, R., Wiel, K. van der, Linden, E. C. van der, Reusen, J., Bogerd, L., Krikken, F., and Selten, F. M.: Strong future increases in Arctic precipitation variability linked to poleward moisture transport, Sci. Adv., 6, eaax6869, https://doi.org/10.1126/sciadv.aax6869, 2020.

Bruhwiler, L., Dlugokencky, E., Masarie, K., Ishizawa, M., Andrews, A. E., Miller, J., Sweeney, C., Tans, P., and Worthy, D.: CarbonTracker-CH4: an assimilation system for estimating emissions of atmospheric methane, Atmospheric Chemistry and Physics, 14, 8269–8293, https://doi.org/10.5194/acp-14-8269-2014, 2014.

Ciais, P., Yao, Y., Gasser, T., Baccini, A., Wang, Y., Lauerwald, R., Peng, S., Bastos, A., Li, W., Raymond, P. A., Canadell, J. G., Peters, G. P., Andres, R. J., Chang, J., Yue, C., Dolman, A. J., Haverd, V., Hartmann, J., Laruelle, G., Konings, A. G., King, A. W., Liu, Y., Luyssaert, S., Maignan, F., Patra, P. K., Peregon, A., Regnier, P., Pongratz, J., Poulter, B., Shvidenko, A., Valentini, R., Wang, R., Broquet, G., Yin, Y., Zscheischler, J., Guenet, B., Goll, D. S., Ballantyne, A.-P., Yang, H., Qiu, C., and Zhu, D.: Empirical estimates of regional carbon budgets imply reduced global soil heterotrophic respiration, Natl Sci Rev, 8, nwaa145-, https://doi.org/10.1093/nsr/nwaa145, 2020.

Crippa, M., Guizzardi, D., Pagani, F., Banja, M., Muntean, M., Schaaf, E., Monforti-Ferrario, F., Becker, W., Quadrelli, R., Risquez-Martin, A., Taghavi-Moharamli, P., Köykkä, J., Grassi, G., Rossi, S., Melo, J., Oom, D., Branco, A., San-Miguel, J., Manca, G., Pisoni, E., Vignati, E., and Pekar, F.: GHG emissions of all world countries, Publications Office of the European Union, Publications Office of the European Union, Luxembourg, 2024.

Etiope, G., Ciotoli, G., Schwietzke, S., and Schoell, M.: Gridded maps of geological methane emissions and their isotopic signature, Earth Sys Sci Data, 11, 1–22, https://doi.org/10.5194/essd-11-1-2019, 2019.

Friedlingstein, P., O'Sullivan, M., Jones, M. W., Andrew, R. M., Hauck, J., Landschützer, P., Quéré, C. L., Li, H., Luijkx, I. T., Olsen, A., Peters, G. P., Peters, W., Pongratz, J., Schwingshackl, C., Sitch, S., Canadell, J. G., Ciais, P., Jackson, R. B., Alin, S. R., Arneth, A., Arora, V., Bates, N. R., Becker, M., Bellouin, N., Berghoff, C. F., Bittig, H. C., Bopp, L., Cadule, P., Campbell, K., Chamberlain, M. A., Chandra, N., Chevallier, F., Chini, L. P., Colligan, T., Decayeux, J., Djeutchouang, L. M., Dou, X., Rojas, C. D., Enyo, K., Evans, W., Fay, A. R., Feely, R. A., Ford, D. J., Foster, A., Gasser, T., Gehlen, M., Gkritzalis, T., Grassi, G., Gregor, L., Gruber, N., Gürses, Ö., Harris, I., Hefner, M., Heinke, J., Hurtt, G. C., Iida, Y., Ilyina, T., Jacobson, A. R., Jain, A. K., Jarníková, T., Jersild, A., Jiang, F., Jin, Z., Kato, E., Keeling, R. F., Goldewijk, K. K., Knauer, J., Korsbakken, J. I., Lan, X., Lauvset, S. K., Lefèvre, N., Liu, Z., Liu, J., Ma, L., Maksyutov, S., Marland, G., Mayot, N., McGuire, P. C., Metzl, N., Monacci, N. M., Morgan, E. J., Nakaoka, S.-I., Neill, C., Niwa, Y., Nützel, T., Olivier, L., Ono, T., Palmer, P. I., Pierrot, D., Qin, Z., Resplandy, L., Roobaert, A., Rosan, T. M., Rödenbeck, C., Schwinger, J., Smallman, T. L., Smith, S. M., Sospedra-Alfonso, R., Steinhoff, T., et al.: Global Carbon Budget 2024, Earth Syst. Sci. Data, 17, 965–1039, https://doi.org/10.5194/essd-17-965-2025, 2025.

This project has received funding from the European Union's Horizon Europe research and innovation programme under grant agreement No 101081395

Hersbach, H., Bell, B., Berrisford, P., Hirahara, S., Horányi, A., Muñoz-Sabater, J., Nicolas, J., Peubey, C., Radu, R., Schepers, D., Simmons, A., Soci, C., Abdalla, S., Abellan, X., Balsamo, G., Bechtold, P., Biavati, G., Bidlot, J., Bonavita, M., Chiara, G. D., Dahlgren, P., Dee, D., Diamantakis, M., Dragani, R., Flemming, J., Forbes, R., Fuentes, M., Geer, A., Haimberger, L., Healy, S., Hogan, R. J., Hólm, E., Janisková, M., Keeley, S., Laloyaux, P., Lopez, P., Lupu, C., Radnoti, G., Rosnay, P. de, Rozum, I., Vamborg, F., Villaume, S., and Thépaut, J.: The ERA5 global reanalysis, Q. J. R. Meteorol. Soc., 146, 1999–2049, https://doi.org/10.1002/qj.3803, 2020.

Houweling, S., Krol, M., Bergamaschi, P., Frankenberg, C., Dlugokencky, E. J., Morino, I., Notholt, J., Sherlock, V., Wunch, D., and Beck, V.: A multi-year methane inversion using SCIAMACHY, accounting for systematic errors using TCCON measurements, Atmospheric Chemistry and Physics, 14, 3991–4012, https://doi.org/10.5194/acp-14-3991-2014, 2014.

ICOS RI, Bergamaschi, P., Colomb, A., De Mazière, M., Emmenegger, L., Kubistin, D., Lehner, I., Lehtinen, K., Leuenberger, M., Lund Myhre, C., Marek, M. V., O'Doherty, S., Platt, S. M., Plaß-Dülmer, C., Apadula, F., Arnold, S., Blanc, P.-E., Brunner, D., Chen, H., ICOS Central Radiocarbon Laboratory. (2024). European Obspack compilation of atmospheric methane data from ICOS and non-ICOS European stations for the period 1984-2024; obspack_ch4_466_GVeu_v10.0_20240729 (Version 10.0) [Data set]. ICOS ERIC - Carbon Portal. https://doi.org/10.18160/PAWA-B2Y4

Jöckel, P., Tost, H., Pozzer, A., Brühl, C., Buchholz, J., Ganzeveld, L., Hoor, P., Kerkweg, A., Lawrence, M. G., Sander, R., Steil, B., Stiller, G., Tanarhte, M., Taraborrelli, D., Aardenne, J. van, and Lelieveld, J.: The atmospheric chemistry general circulation model ECHAM5/MESSy1: consistent simulation of ozone from the surface to the mesosphere, Atmos. Chem. Phys., 6, 5067–5104, https://doi.org/10.5194/acp-6-5067-2006, 2006.

Johnson, M. S., Matthews, E., Du, J., Genovese, V., and Bastviken, D.: Methane Emission From Global Lakes: New Spatiotemporal Data and Observation-Driven Modeling of Methane Dynamics Indicates Lower Emissions, J Geophys Res Biogeosciences, 127, e2022JG006793, https://doi.org/10.1029/2022jg006793, 2022.

Kaiser, J. W., Heil, A., Andreae, M. O., Benedetti, A., Chubarova, N., Jones, L., Morcrette, J.-J., Razinger, M., Schultz, M. G., Suttie, M., and Werf, G. R. van der: Biomass burning emissions estimated with a global fire assimilation system based on observed fire radiative power, Biogeosciences, 9, 527–554, https://doi.org/10.5194/bg-9-527-2012, 2012.

Krol, M., Houweling, S., Bregman, B., Broek, van den M., Segers, A., Velthoven, P. van, Peters, W., Dentener, F., and Bergamaschi, P.: The two-way nested global chemistry-transport zoom model TM5: algorithm and applications, Atmospheric Chemistry and Physics, 5, 417–432, https://doi.org/10.5194/acp-5-417-2005, 2005.

Meirink, J. F., Bergamaschi, P., and Krol, M. C.: Four-dimensional variational data assimilation for inverse modelling of atmospheric methane emissions: method and comparison with synthesis inversion, Atmospheric Chemistry and Physics, 8, 6341–6353, https://doi.org/10.5194/acp-8-6341-2008, 2008.

Peters, W., Miller, J. B., Whitaker, J., Denning, A. S., Hirsch, A., Krol, M. C., Zupanski, D., Bruhwiler, L., and Tans, P. P.: An ensemble data assimilation system to estimate CO 2surface fluxes from atmospheric trace gas observations, J. Geophys. Res., 110, 419–21, https://doi.org/10.1029/2005jd006157, 2005.

Piao, S., Friedlingstein, P., Ciais, P., Viovy, N., and Demarty, J.: Growing season extension and its impact on terrestrial carbon cycle in the Northern Hemisphere over the past 2 decades, Glob. Biogeochem. Cycles, 21, https://doi.org/10.1029/2006gb002888, 2007.

This project has received funding from the European Union's Horizon Europe research and innovation programme under grant agreement No 101081395

Rantanen, M., Karpechko, A. Yu., Lipponen, A., Nordling, K., Hyvärinen, O., Ruosteenoja, K., Vihma, T., and Laaksonen, A.: The Arctic has warmed nearly four times faster than the globe since 1979, Commun. Earth Environ., 3, 168, https://doi.org/10.1038/s43247-022-00498-3, 2022.

Rocher-Ros, G., Stanley, E. H., Loken, L. C., Casson, N. J., Raymond, P. A., Liu, S., Amatulli, G., and Sponseller, R. A.: Global methane emissions from rivers and streams, Nature, 621, 530–535, https://doi.org/10.1038/s41586-023-06344-6, 2023.

Sasakawa, M., Shimoyama, K., Machida, T., Tsuda, N., Suto, H., Arshinov, M., Davydov, D., Fofonov, A., Krasnov, O., and Saeki, T.: Continuous measurements of methane from a tower network over Siberia, Tellus B, 62, 403–416, https://doi.org/10.1111/j.1600-0889.2010.00494.x, 2010.

Saunois, M., Martinez, A., Poulter, B., Zhang, Z., Raymond, P. A., Regnier, P., Canadell, J. G., Jackson, R. B., Patra, P. K., Bousquet, P., Ciais, P., Dlugokencky, E. J., Lan, X., Allen, G. H., Bastviken, D., Beerling, D. J., Belikov, D. A., Blake, D. R., Castaldi, S., Crippa, M., Deemer, B. R., Dennison, F., Etiope, G., Gedney, N., Höglund-Isaksson, L., Holgerson, M. A., Hopcroft, P. O., Hugelius, G., Ito, A., Jain, A. K., Janardanan, R., Johnson, M. S., Kleinen, T., Krummel, P. B., Lauerwald, R., Li, T., Liu, X., McDonald, K. C., Melton, J. R., Mühle, J., Müller, J., Murguia-Flores, F., Niwa, Y., Noce, S., Pan, S., Parker, R. J., Peng, C., Ramonet, M., Riley, W. J., Rocher-Ros, G., Rosentreter, J. A., Sasakawa, M., Segers, A., Smith, S. J., Stanley, E. H., Thanwerdas, J., Tian, H., Tsuruta, A., Tubiello, F. N., Weber, T. S., Werf, G. R. van der, Worthy, D. E. J., Xi, Y., Yoshida, Y., Zhang, W., Zheng, B., Zhu, Q., Zhu, Q., and Zhuang, Q.: Global Methane Budget 2000–2020, Earth Syst. Sci. Data, 17, 1873–1958, https://doi.org/10.5194/essd-17-1873-2025, 2025.

Schepaschenko, D., Moltchanova, E., Fedorov, S., Karminov, V., Ontikov, P., Santoro, M., See, L., Kositsyn, V., Shvidenko, A., Romanovskaya, A., Korotkov, V., Lesiv, M., Bartalev, S., Fritz, S., Shchepashchenko, M., and Kraxner, F.: Russian forest sequesters substantially more carbon than previously reported, Sci Rep-uk, 11, 12825, https://doi.org/10.1038/s41598-021-92152-9, 2021.

Schuldt, K. N., Aalto, T., Andrade, M., Arlyn Andrews, Apadula, F., Jgor Arduini, Arnold, S., Baier, B., Bäni, L., Bartyzel, J., Bergamaschi, P., Biermann, T., Biraud, S. C., Pierre-Eric Blanc, Boenisch, H., Brailsford, G., Brand, W. A., Brunner, D., Bui, T. P. V., Miroslaw Zimnoch. (2024). Multi-laboratory compilation of atmospheric carbon dioxide data for the period 1983-2023; obspack_ch4_1_GLOBALVIEWplus_v7.0_2024-10-29 [Data set]. NOAA Global Monitoring Laboratory. https://doi.org/10.25925/20241001

Shvidenko, A., Ciais, P., Patra, P. K., Bastos, A., Maksyutov, S., Lauerwald, R., Poulter, B., Belikov, D., Chandra, N., Glagolev, M., Terentieva, I., Karelin, D., Kurbatova, J., Kurganova, I., Romanovskaya, A., Korotkov, V., Mukhortova, L., Prokushkin, A., Gustafson, E., Kraxner, F., Mamkin, V., Lukina, N., Krasovskiy, A., Vaganov, E., and Schepaschenko, D.: A System Reanalysis of the Current Greenhouse Gases Budget of Terrestrial Ecosystems in Russia, Glob. Biogeochem. Cycles, 39, https://doi.org/10.1029/2025gb008540, 2025.

Spivakovsky, C. M., Logan, J. A., Montzka, S. A., Balkanski, Y. J., Foreman-Fowler, M., Jones, D. B. A., Horowitz, L. W., Fusco, A. C., Brenninkmeijer, C. A. M., and Prather, M. J.: Three-dimensional climatological distribution of tropospheric OH: Update and evaluation, Journal of Geophysical Research: Atmospheres, 105, 8931–8980, https://doi.org/10.1029/1999jd901006, 2000.

Tenkanen, M. K., Tsuruta, A., Gon, H. D. van der, Höglund-Isaksson, L., Leppänen, A., Markkanen, T., Petrescu, A. M. R., Raivonen, M., Aaltonen, H., and Aalto, T.: Partitioning anthropogenic and natural methane emissions in Finland during 2000–2021 by combining bottom-up and top-down estimates, Atmos. Chem. Phys., 25, 2181–2206, https://doi.org/10.5194/acp-25-2181-2025, 2024.

This project has received funding from the European Union's Horizon Europe research and innovation programme under grant agreement No 101081395

Thompson, R. L. and Stohl, A.: FLEXINVERT: an atmospheric Bayesian inversion framework for determining surface fluxes of trace species using an optimized grid, Geosci Model Dev, 7, 2223–2242, https://doi.org/10.5194/gmd-7-2223-2014, 2014.

Tsuruta, A., Aalto, T., Backman, L., Hakkarainen, J., Laan-Luijkx, I. T. van der, Krol, M. C., Spahni, R., Houweling, S., Laine, M., Dlugokencky, E., Gomez-Pelaez, A. J., Schoot, M. van der, LANGENFELDS, R., Ellul, R., Arduini, J., Apadula, F., Gerbig, C., Feist, D. G., Kivi, R., Yoshida, Y., and Peters, W.: Global methane emission estimates for 2000–2012 from CarbonTracker Europe-CH_4 v1.0, Geoscientific Model Development, 10, 1261–1289, https://doi.org/10.5194/gmd-10-1261-2017, 2017.

Tsuruta, A., Aalto, T., Backman, L., Krol, M. C., Peters, W., Lienert, S., Joos, F., Miller, P. A., Zhang, W., Laurila, T., Hatakka, J., Leskinen, A., Lehtinen, K. E. J., Peltola, O., Vesala, T., Levula, J., Dlugokencky, E., Heimann, M., Kozlova, E., Aurela, M., Lohila, A., Kauhaniemi, M., and Gomez-Pelaez, A. J.: Methane budget estimates in Finland from the CarbonTracker Europe-CH 4 data assimilation system, Tellus B Chem Phys Meteorology, 71, 1565030, https://doi.org/10.1080/16000889.2018.1565030, 2019.

Weber, T., Wiseman, N. A., and Kock, A.: Global ocean methane emissions dominated by shallow coastal waters, Nature communications, 10, 1–10, https://doi.org/10.1038/s41467-019-12541-7, 2019.

Yang, H., Ciais, P., Frappart, F., Li, X., Brandt, M., Fensholt, R., Fan, L., Saatchi, S., Besnard, S., Deng, Z., Bowring, S., and Wigneron, J.-P.: Global increase in biomass carbon stock dominated by growth of northern young forests over past decade, Nat. Geosci., 16, 886–892, https://doi.org/10.1038/s41561-023-01274-4, 2023.

This project has received funding from the European Union's Horizon Europe research and innovation programme under grant agreement No 101081395

https://eyeclima.eu

BRUSSELS, 02 03 2026

Funded by the European Union. Views and opinions expressed are however those of the author(s) only and do not necessarily reflect those of the European Union. Neither the European Union nor the granting authority can be held responsible for them.

This project has received funding from the European Union's Horizon Europe research and innovation programme under grant agreement No 101081395